

1a. REPORT SECURITY CLASSIFICATION

2a. SECURITY CLASSIFICATION AUTHORITY

2b. DECLASSIFICATION / DOWNGRADING SCHEDULE

4. PERFORMING ORGANIZATION REPORT NUMBER(S)

6a. NAME OF PERFORMING ORGANIZATION
Univ. of Arkansas for Med. Sci.
NMR Laboratory6c. ADDRESS (City, State, and ZIP Code)
4301 West Markham Street
Little Rock, AR 722058a. NAME OF FUNDING/SPONSORING
ORGANIZATION
Office of Scientific Research8c. ADDRESS (City, State, and ZIP Code)
Building 410
Bolling AFB, D.C. 20332-64486b. OFFICE SYMBOL
(If applicable)8b. OFFICE SYMBOL
(If applicable)6d. AFOSCD TO
5

1b. RESTRICTIVE MARKINGS

3. DISTRIBUTION/AVAILABILITY OF REPORT

unlimited

5. MONITORING ORGANIZATION REPORT NUMBER(S)

7a. NAME OF MONITORING ORGANIZATION
Same as Sa7b. ADDRESS (City, State, and ZIP Code)
Same as 8c

9. PROCUREMENT INSTRUMENT IDENTIFICATION NUMBER

AFOSR-89-0418

10. SOURCE OF FUNDING NUMBERS

PROGRAM ELEMENT NO.	PROJECT NO.	TASK NO.	WORK UNIT ACCESSION NO.
61102F	2301	A3	

11. TITLE (Include Security Classification)

NMR IMAGING OF ELASTOMERIC MATERIALS

12. PERSONAL AUTHOR(S)

Komoroski, Richard Andrew; Sarkar, Subhendra N.; Wooten, E. Wrenn

13a. TYPE OF REPORT
Final13b. TIME COVERED
FROM 89/07/01 TO 92/06/3014. DATE OF REPORT (Year, Month, Day)
92/08/3115. PAGE COUNT
42

16. SUPPLEMENTARY NOTATION

4 published papers included.

17. COSATI CODES		
FIELD	GROUP	SUB-GROUP

18. SUBJECT TERMS (Continue on reverse if necessary and identify by block number)

nuclear magnetic resonance, imaging, elastomers, tires, defects, composites, spin echo, Lithium-7, fluorine-19, carbon black, interfaces, curing, filler, NMR imaging, relaxation coke

19. ABSTRACT (Continue on reverse if necessary and identify by block number)

NMR imaging has been applied to elastomeric materials of industrial and military interest. The T₂ spin-spin relaxation times of common elastomers, particularly after filling and curing, are sufficiently short that spin-echo sequences at submillisecond echo times cannot produce T₂-independent images. The sensitivity to T₂ makes spin echo imaging a good probe of elastomer blend composition, as demonstrated for a series of filled, cured cis-polybutadiene, styrene-butadiene rubber blends. The technique can distinguish good and bad carbon black dispersion in actual tire tread samples. The configuration of non-metallic tire cord, voids, rubber layer boundaries, apparent migration of additives, and other inhomogeneities can be detected in end-product tire samples. Arrowhead patterns, arising from magnetic susceptibility differences for defects in carbon-black-filled elastomers, were attributed to graphitized "coke" particles from the carbon black. NMR images were obtained for porous glass disks of different porosities as models of materials such as oil cores. The mottled appearance often seen for such images is attributed largely to insufficient signal-to-noise

20. DISTRIBUTION/AVAILABILITY OF ABSTRACT

 UNCLASSIFIED/UNLIMITED SAME AS RPT DTIC USERS

21. ABSTRACT SECURITY CLASSIFICATION

Unclass

22a. NAME OF RESPONSIBLE INDIVIDUAL

Komoroski

22b. TELEPHONE (Include Area Code)

212-767-1933

22c. OFFICE SYMBOL

LC

Block 19.

ratio, and not pore structures. Comparison of spin-echo and gradient-echo images demonstrates the defect-magnification effect of the gradient-echo sequence seen previously for elastomers. The advantages of volume imaging, isotropic voxels in thin slices, and higher resolution are demonstrated for porous materials. Images with isotropic voxels of 80-100 μm on a side were obtained in several hours. Dramatic differences are not seen at 100 μm resolution for disks of average pore size 15 to 200 μm because the images are dominated by the large-pore tail of the size distribution.

Accession For	
NTIS GRA&I	<input checked="" type="checkbox"/>
DTIC TAB	<input type="checkbox"/>
Unarmoured	<input type="checkbox"/>
Justification	
By _____	
Distribution/	
Availability Codes	
Dist R/1	Avail and/or
	Special

NMR Imaging of Composition and Defects in Industrial Elastomers

Richard A. Komoroski and Subhendra N. Sarkar

Departments of Radiology and Pathology, University of Arkansas for Medical Sciences, 4301 W. Markham St., Little Rock, AR 72205, USA

Introduction

Nuclear magnetic resonance (NMR) imaging is a promising tool for noninvasive mapping of spatial structures in materials [1]. Until now it has been applied with some success to highly mobile phases in porous systems [2, 3]. Applications to rigid solids and polymers are just beginning. Elastomers, having partially narrowed lines due to polymer chain segmental motions [4], create an intermediate situation for imaging compared to other materials.

NMR imaging of polymers and composites can reveal relatively large mechanical details (currently tens of microns in size) of composite layers, filler dispersion, size and morphology of defects [5-7], and perhaps provide physicochemical information regarding crystallinity, adhesion, compatibility of phases in blend mixing [7, 8], etc.

A major focus of present day materials imaging research is on difficult-to-image rigid materials. Glassy or crystalline materials have very short T_2 and large line-widths. Imaging with magic angle spinning (MAS) [9] is not readily feasible for irregular samples and creates deformation of elastomers. Multiple pulse line narrowing methods require fast switching of gradients, intense pulses, and very demanding hardware [10, 11]. However, it is not clear how effective line-narrowing sequences will be for elastomers, where the dipolar line width is strongly narrowed by chain segmental motion [4]. In some cases an alternative is to increase the temperature of the sample [12].

To achieve low TE sequences it is necessary to stretch the current limitations of medical NMR imaging. Submillisecond TE s have been obtained by employing strong, actively shielded gradients capable of fast switching (50-100 μ s) in a modified whole volume 3D-NMR imaging sequence in intermediate-size magnet bores (10-25 cm) capable of accommodating larger samples than standard high resolution NMR systems.

419664
92-26585 48
PZ

92 10 8 066

Literature Review

Two-dimensional spin echo imaging of industrial elastomers and blends well above their T_g [5, 6] has addressed various aspects of imageability, including specific applicability of gradient-echo imaging in preference to spin-echo methods for detection of material defects, detectability of elastomer edges below pixel resolution, and the need to use higher gradient strengths with low TE sequences for the morphology and composition of common industrial blends.

Elevated temperatures [12] produce greater polymer segmental mobility and give narrower lines and improved S/N for imaging of rigid polymers like nylon. However, elevated temperature can change polymer structure and morphology permanently and cannot always be classed as a nondestructive technique.

In cases where NMR peaks from different phases or from different molecular environments can be resolved, chemical shift selective excitation may produce helpful discrimination of physical or molecular components in an NMR image. This has been suggested by selectively exciting the unsaturated 1H peak in a polybutadiene/polydimethylsiloxane mixture [13].

Inhomogeneities like voids or highly cross-linked regions have been imaged using ingressed solvents in vulcanized rubber [14] and polybutadiene [15–17]. However, ambiguities in 1H quantitation and regional T_2 variations may accompany the presence of solvent. The use of mobile penetrants in rubbers is invasive and can cause differential swelling and dimensional changes, making image interpretation difficult. Cords have been distinguished in V-belts presoaked in H_2O by imaging the ingress of water [18].

Direct imaging of low concentrations of polymeric binder distribution in green ceramics [19] by both 2D and 3D spin-echo imaging at TE 's of 2 to 6 ms has resulted in unambiguous visualization of the organic phase. The same group has imaged the organic phase in silica reinforced polydimethylsiloxane composites [20] having heterogeneous distributions of partially hydrolyzed tetraethyl orthosilicate. Due to the very low $^1H T_2$ for the major fraction of such a polymer network, the TE used is still about 4 T_2 or higher and the spin-echo images visualize only 3–5% of the available protons. Although such images can yield valuable information, an accurate mapping of various phases in these low T_2 systems may require submillisecond TE imaging sequences.

Spin echo NMR imaging has been applied to study segmental mobility of an aged polymer network and to observe the kinetics of growth of a highly crosslinked surface layer in vulcanized natural rubber [21]. Phase segregation in a stearic acid/paraffin mixture and phase separation in a polyisoprene/polystyrene blend were also observed from changes in NMR images [21].

Tire Materials and Model Elastomers

We describe here NMR images of several tire sections which demonstrate visualization of composite elastomeric layers of varying composition, tire cords, and differences in dispersion of carbon black in finished tire tread. Images of model diblends yield an estimate of the sensitivity of the technique to elastomer compositional changes. Separately cured elastomer sheets with identical T_2 can be distinguished even with no physical separation between them. Finally, possible origins of intensity artifacts in filled elastomers are discussed.

3D NMR Imaging of Tire Sections

Figure 1(a) shows a typical central slice from a set of 32 contiguous sagittal slices of a tire section manufactured from 60 phr carbon black loaded, cured natural rubber and imaged with a 3D whole volume imaging sequence at a TE of 900 μ s with image resolution of $1 \times 1 \times 2 \text{ mm}^3$. Treads, layer structure, and a few defects are visible in this slice. The fuzziness at the edges is due to low resolution. Figure 1(b) is one of four 1-mm thick slices selected from the center of the same tire by a partial volume (thick slab) imaging sequence with a higher in-plane resolution ($0.5 \times 0.5 \text{ mm}^2$) at a TE of 1.9 ms. Note that considerably more details from various layers, including visualization of cord boundaries, are available after a marginal improvement in resolution.

Figure 2(a) shows a typical transverse slice (from a set of 16, each 20 μm thick) of a 3D NMR image at a TE of 1.9 ms for a non-steel-belted, bias-ply tire cross section [7]. The tread is to the left and the interior portion of the tire to the right. At the in-plane resolution of 100 μm , the tread layer at left can be distinguished from the second region of higher intensity containing embedded rigid fibers appearing as dark spots in each slice. The layer boundary as well as the fiber-rubber interfaces are well defined. In the T_2 -weighted images, the fibers yield no signal because of very short T_2 associated with the absence of substantial molecular motion. A 2-mm thick layer at the rightmost side, which visually appears no different from the leftmost layer, is barely visible in this image. Numerous other defects, presumably voids, chunks of carbon black or other material, and broken or misaligned fibers are also present in these images. Some of the defects display a characteristic arrowhead pattern of bright spots pointing along the frequency encode direction [6-8, 22]. This pattern results from magnetic susceptibility differences between defects and surrounding matrix, and is described in more detail later.

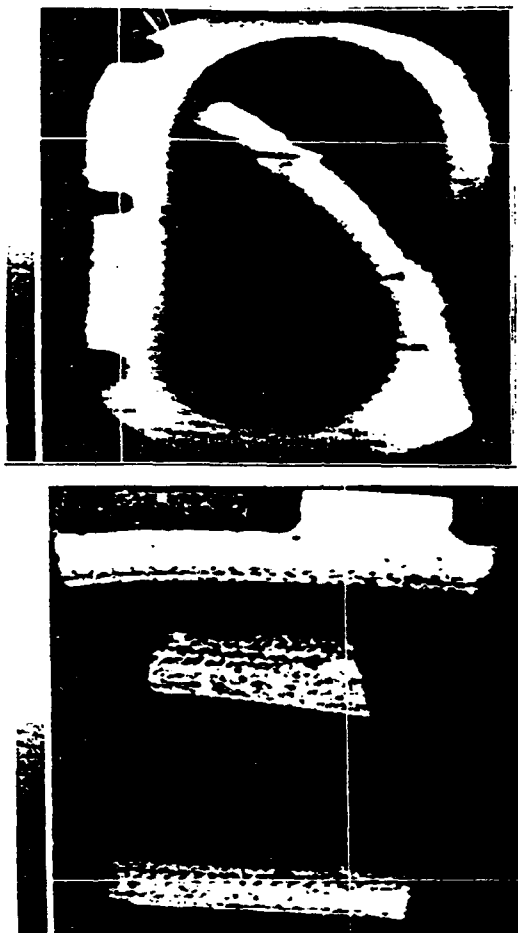


Figure 1. (a) Typical longitudinal ^1H image slice from a 3D set of 32 slices of filled and cured NR tire at $1 \times 1 \times 2 \text{ mm}^3$ resolution. TE , 0.9 ms. (b) Typical transverse slice of the same section at $0.5 \times 0.5 \times 1 \text{ mm}^3$ resolution obtained with a partial volume imaging sequence at a TE of 1.9 ms.

A coarser image of a thicker slice ($200 \times 200 \times 500 \mu\text{m}^3$ resolution, TE 750 μs) from the same region has been burned-in to clearly show the presence of the rightmost layer (Fig. 2(b)), which is more clearly defined as two layers in the profile at bottom. The combination of shorter TE and coarser resolution has enhanced the visibility of this feature. Scalar decoupled ^{13}C MAS spectra at 75.57 MHz have been obtained for each of the four layers. The outermost layer (tread) and the middle layer containing fibers correspond to *cis*-polysisoprene (NR)/*cis*-polybutadiene (*cis*-BR) emulsion styrene butadiene rubber (SBR) blends in the approximate ratios of 20/10/70 and 40/10/50, respectively; the right layer immediately adjacent to the fiber-containing region corresponds to a small amount of NR blended with butyl rubber; and the rightmost layer (closest to the enclosed air in a tubeless tire) corresponds to primarily butyl rubber [23]. Although the T_g of butyl rubber is -70°C , its polymer chain segmental mobility is substantially restricted relative to elastomers

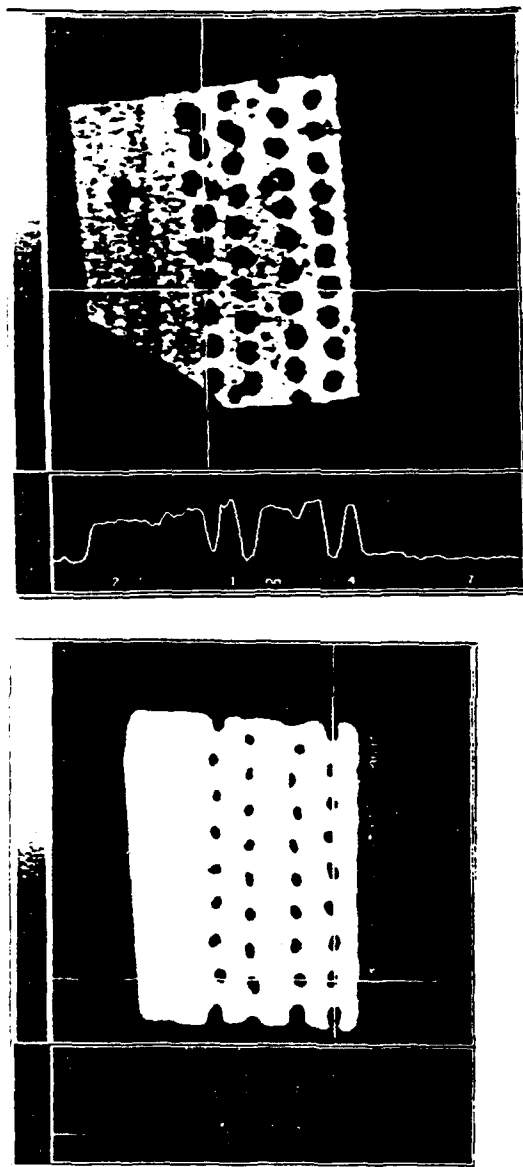


Figure 2. (a) Typical horizontal slice from sixteen 3D whole volume images of a bias-ply tire. $TE = 1.9$ ms; resolution $100 \times 100 \times 200 \mu\text{m}^3$. (b) $500\text{-}\mu\text{m}$ thick slice ($TE = 750 \mu\text{s}$) at $200 \mu\text{m}$ in-plane resolution with intensity burned in to highlight the presence of two weak layers on right.

of similar T_g . Thus, with a shorter ^1H T_2 (<0.1 ms) than other common elastomers, butyl rubber is more difficult to detect in NMR images. The addition of some *cis*-polyisoprene rubber would increase the ^1H T_2 of that layer, making it slightly more intense on the NMR image.

The image-guided destructive analysis by ^{13}C MAS NMR can offer further information supporting the nondestructive and quick observation available through NMR imaging. Bulk spectral or spin relaxation measurements obviously cannot provide

the spatial detail nondestructively. The detailed composite nature of the tire tread as a whole is completely obscured in the values of ^1H NMR T_2 s and line widths in Table 1.

NMR Imaging of *cis*-BR/SBR Model Diblends

Application of NMR imaging to nondestructive characterization of material composition, particularly for composite elastomer systems, may require some type of calibration curve from the images of simpler, well characterized components which comprise the whole composite system. Imaging of *cis*-BR/SBR diblends of known composition demonstrates such an approach for an important class of elastomeric composites.

Six model sheets of *cis*-BR/SBR have been studied in detail [7]. Transverse relaxation times and line widths for each of the sheets and for the combined stack of all sheets are given in Table 1. The increase in T_1 values with increasing SBR content is slight [7]. The change in line width with increasing SBR content (Table 1) tells little about the blends.

On the other hand, T_2 decreases steadily and substantially with increasing SBR content, which is a consequence of the decreased low frequency segmental mobility of SBR (T_g of SBR = -55°C ; T_g of *cis*-BR = -102°C). The relative uniformity in ^1H density for these sheets [7] leaves the variation in T_2 as the prime cause of the image intensity variations (Figure 3(a, b)). Note that measurement of NMR parameters from the composite stack of all six sheets together tells nothing about composition variations locally or in the individual sheets.

Figure 3(a) shows a typical NMR image from a 16-slice, 3D dataset with $200 \times 200 \times 500 \mu\text{m}^3$ resolution for the six model *cis*-BR/SBR blend sheets at a TE of 1.1 ms. Figure 3(b) shows an image slice of the same sheets at better resolution ($100 \times 100 \times 250 \mu\text{m}^3$) with a sacrifice in echo time ($TE = 2$ ms due to the larger data acquisition time), and the corresponding loss in S/N ratio. As the SBR content increases, the image intensities decrease in both images in regular fashion as expected. This is also evident in the intensity profiles projected on the right sides. The results in Figure 3 demonstrate the ability of NMR imaging to exquisitely differentiate polymer blend compositions based on T_2 differences. Clearly the use of a very short TE brings about a substantial improvement in our ability to detect the high-SBR-content sheets as it did for the butyl rubber layers of the tire section. The degree of differentiation depends on the variation in T_2 and the TE used. However, at the lowest TE obtained in this system (0.5 ms, not shown here), we could not remove the

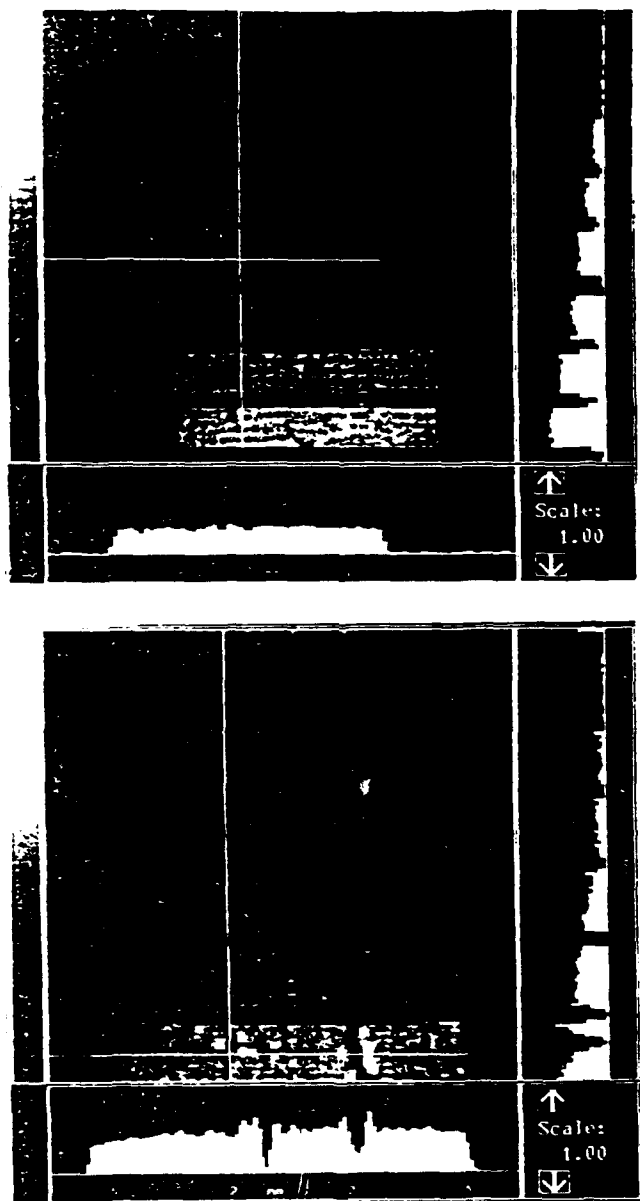


Figure 3. (a) A 500- μm slice from a 16-slice noninterpolated volume data set of six model diblock sheets of *cis*-BR(SBR with composition ratios 100:0, 80:20, 60:40, 40:60, 20:80 and 0:100 (bottom to top) at 200 μm in-plane resolution. TE , 1 ms. (b) 250- μm slice from a 32-slice noninterpolated volume data set of the same sheets at lower field of view. Resolution, $100 \times 100 \mu\text{m}^2$. TE , 2 ms.

effect of T_2 for these typical elastomers. In a T_2 -independent image all six sheets would be of approximately equal intensity, and at a $TE > 5$ ms the sheets with high SBR content (having T_2 s < 500 μ s) will be barely visible in the NMR images. In this collection of model diblends, the T_2 variation was at least 100 μ s (10% of the TE used) between two adjacent sheets differing by 20% in SBR content. One can perhaps detect as little as 10% variation in the BR/SBR composition with the above 3D imaging modality.

Detectability of Elastomer Edges

In early work on separately cured *cis*-BR sheets [5] separated by spacings of various widths, sub-pixel-size separations were detectable even at a poor resolution (about 500 μ m in-plane) and long TE (12 ms). Figure 4 shows a higher resolution ($80 \times 80 \times 500$ μ m 3) image of the same sheets at a TE comparable to the T_2 (4 ms) with 180- μ m glass spacers at two boundaries and with no spacer at the third boundary [6]. Note that all three boundaries are detectable. The T_2 does not vary from the bulk to the surface as measured using intensities from a row of voxels as a function of TE . This suggests that boundaries between separately cured rubber sheets with no difference in T_2 are distinguishable more easily than co-cured interfaces in tire treads, since distinction of co-cured edges may require T_2 variation at least of the order of 10% of the TE used, as demonstrated by the model diblends above.

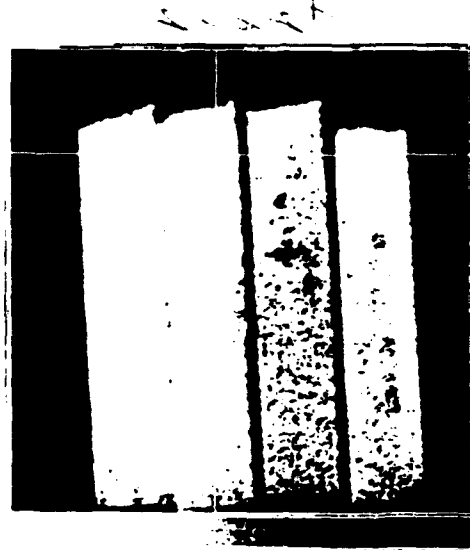


Figure 4. A 500- μ m slice from a 8-slice volume data set for 4 cured, filled 2-mm *cis*-BR sheets at 80 μ m in-plane resolution. The bottom three sheets are separated by two 180- μ m thick glass spacers. The top two sheets have no spacer. TE , 4.3 ms.

Detection of Filler Dispersions in Tire Treads

The mechanical properties of tire tread depend strongly on the degree of carbon black dispersion, among other things. Carbon black dispersion is typically measured at the surface by mechanical [24] or photometric techniques such as AMEDA [25]. There is no nondestructive way to characterize carbon black dispersion locally deep within a sample.

Figure 5 shows typical images from two finished tire tread sections – one with good and the other with poor carbon black dispersion [7]. Tread grooves are well

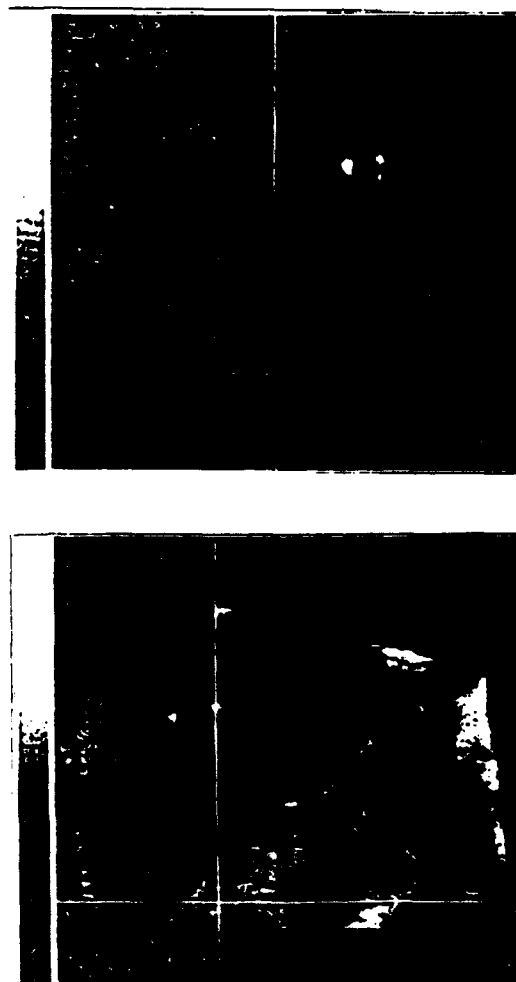


Figure 5. (a) Typical NMR image from an experimental tire tread with good dispersion of carbon black at $150 \times 150 \times 350 \mu\text{m}^3$ resolution. (b) NMR image of an experimental tire tread with poor carbon black dispersion. TE , 1.3 ms for both tires.

Table 1. NMR transverse relaxation times and linewidths of tire tread sections and BR/SBR model diblends.

Tire or BR/SBR diblend samples	Line width (Hz)	T_2 (μs)
Bias-ply tire	1850	< 100*, 950
Exptl tire with poor filler dispersion	2600	(60%) 1000 (40%) 630
Exptl tire with good filler dispersion	1400	1100
Uncured, unfilled <i>cis</i> -BR	150	1100, 4000*
Uncured, unfilled <i>s</i> -SBR (BR : SBR wt% in diblends)	550	500, 6000*
100 : 0	650	1000
80 : 20	600	880
60 : 40	650	730
40 : 60	750	620
20 : 80	820	500
0 : 100	980	50 – 150
6 blends together	1200	750

* Minor component of T_2 responsible for 10% of total intensity.

defined in both sections. The relatively even appearance in Figure 5(a) is consistent with well dispersed carbon black, although the section is not defect-free. The image of Figure 5(b) displays a highly uneven appearance, consisting of regions of poor dispersion of several hundred microns diameter detectable at 150 μm in-plane resolution. Note that the T_2 measurements on the sections gave two values of T_2 for the poor dispersion sample, as compared to a single value of T_2 for the good dispersion sample (Table 1). A fraction of polymer in the poor dispersion section has a substantially reduced T_2 , resulting in a signal loss at constant *TE*. This fraction may represent bound rubber. This is another example where the two results together provided more information than NMR imaging or relaxation parameters alone.

Magnetic Susceptibility Artifacts in NMR Images

In most of the images shown above, defects surrounded by three bright spots in an arrowhead configuration appear along the frequency encode direction. This pattern is common in the NMR images of carbon black filled elastomers. An extreme case for cured, 40 phr carbon black loaded natural rubber is shown in Figure 6(a) at a resolution of $100 \times 100 \times 200 \mu\text{m}^3$. Among the possible sources which may produce this pattern are voids, particles of metal or other foreign material, or agglo-

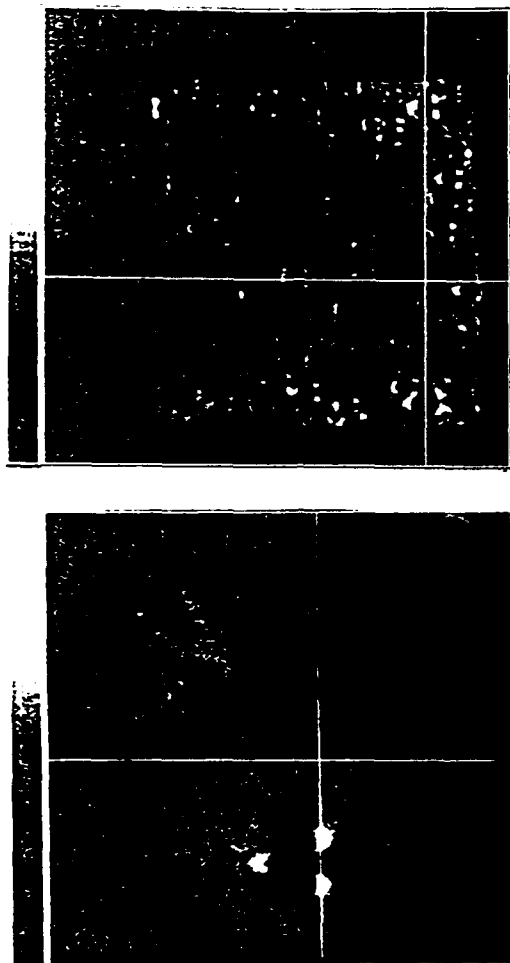


Figure 6. (a) Typical 200- μm image slice at $100 \times 100 \mu\text{m}^2$ in-plane resolution of cured, filled natural rubber from a 3D volume data set at TE 2 ms. Note the occurrence of many randomly distributed intensity artifacts. (b) Typical spin-echo, volume image slice of a phantom containing a capillary filled with air (top right), a capillary filled with powdered carbon black (close to center), a graphite pencil tip (lower center), and air pockets visible as irregular defects in a vegetable shortening matrix. Note the arrowhead artifact occurring around the pencil tip. TE , 1.3 ms.

merates of carbon black. We suspect that the artifacts arise primarily from particulate carbon black in crystalline or graphitic phase ("coke"), which is produced in the carbon black manufacturing process and is present in the filled elastomer after the mixing step [25].

Crystalline carbon black should result in a large magnetic susceptibility difference relative to the surrounding filled elastomer. As a test of this hypothesis, Figure 6(b) shows a typical volume image of a phantom consisting of a glass capillary filled with air (top right), another glass capillary filled with powdered carbon black (close to center) and a graphite pencil tip (lower center) embedded in a matrix of commercial vegetable shortening. Additional irregular air pockets are also visible. Carbon black was also mixed directly into the top region of the shortening.

No prominent magnetic susceptibility artifacts are seen at any of the air pockets or either glass capillary. A prominent arrowhead artifact appears only at the graphite

tip. By applying the gradient-echo sequence, which is sensitive to T_2^* , the arrowhead pattern is washed away, and the defect region containing the pencil tip becomes enlarged (not shown here). This supports our interpretation of the large susceptibility variation as the origin of such artifacts. "Coke" particles are the most likely cause, although small iron or rust particles or perhaps particulate carbon black agglomerates cannot be ruled out totally.

Summary

Direct T_2 -weighted, low TE spin-echo NMR imaging can visualize certain morphologic and defect structures, and can differentiate among various layers in actual tire samples with no probing agent. At a gradient strength of 20 G/cm and a TE of about 1 ms, the T_2 weighted 3D images can differentiate *cis*-BR/SBR diblends which vary in molecular composition by 10–20%. Edges of separately cured elastomers with identical T_2 can be resolved. Tire treads having differences in carbon black mixing can be differentiated at medium (150 μ m) resolution. Short echo times dramatically improve image quality, and the multislice 3D imaging sequence is a valuable approach for imaging real elastomeric composites, although T_2 weighting is still present in the images of common elastomers. Magnetic susceptibility artifacts frequently appear in the images of filled elastomers, and may be a means for identifying various defects based on their magnetic susceptibility differences.

Acknowledgments

We thank Ken Schur of the Uniroyal-Goodrich Tire Company and Jim Visintainer of Goodyear Tire Company for providing samples and for stimulating discussions. This research was funded by grant AFOSR-89-0418 from the Air Force Office of Scientific Research.

References

[1] Listerud, J.M., Sinton, S.W., Drobny, G.P., *Anal. Chem.* 1989, 61, 23A.

[2] Sarkar, S.N., Wooten, E.W., Komoroski, R.A., *Appl. Spectrosc.* 1991, 45, 619, and references therein.

[3] Dechter, J.J., Komoroski, R.A., Ramaprasad, S., *J. Magn. Reson.* 1991, 93, 142.

[4] Komoroski, R.A., in *High Resolution NMR Spectroscopy of Synthetic Polymers in Bulk*: Komoroski, R.A. (ed.) VCH Publishers: Deerfield Beach, Florida, 1986: Ch. 4.

[5] Chang, C., Komoroski, R.A., *Macromolecules* 1989, 22, 600.

[6] Komoroski, R.A., Sarkar, S.N., *Proc. Mat. Res. Soc.* 1991, 217, 3.

[7] Sarkar, S.N., Komoroski, R.A., *Macromolecules* 1991, submitted. *1/2/92, -5, 1725*

[8] Sarkar, S.N., Visintainer, J., Komoroski, R.A., unpublished work.

[9] Cory, D.G., deBoer, J.C., Veeman, W.S., *Macromolecules* 1989, 22, 1618.

[10] Miller, J.B., *Trends Anal. Chem.* 1991, 10, 59.

[11] Cory, D.G., Miller, J.B., Turner, R., Garroway, A.N., *Mol. Phys.* 1990, 70, 331. *1/2/92, 1, 1725*

[12] Jezzard, P., Carpenter, T.A., Hall, L.D., *J. Polym. Commun.* 1991, 32, 74. *1/2/92, 1, 1725*

[13] Garrido, L., Mark, J.E., *ACS Polym. Preprints* 1989, 30 (#2), 217.

[14] Webb, A.G., Jezzard, P., Hall, L.D., Ng, S., *Polym. Commun.* 1989, 30, 363.

[15] Weisenberger, L.A., Koenig, J.L., *Appl. Spectrosc.* 1989, 43, 1117.

[16] Clough, R.S., Koenig, J.L., *J. Polym. Sci. Polym. Lett.* 1989, 27, 451.

[17] Smith, S.R., Koenig, J.L., *Macromolecules* 1991, 24, 3496.

[18] Kormos, D.W., Kapadia, R.D., Ritchey, W.M., *31st Experimental NMR Spectrosc. Conf. Asilomar, CA, April 1990, Abstracts*, p 188.

[19] Garrido, L., Ackerman, J.C., Ellingson, W.A., *J. Magn. Reson.* 1990, 88, 340.

[20] Garrido, L., Marks, J.E., Sun, C.C., Ackerman, J.L., Chang, C., *Macromolecules* 1991, 24, 4067.

[21] Blümller, P., Blümlich, B., *Macromolecules* 1991, 24, 2183.

[22] Ludeke, K.M., Roschmann, P., Tischler, R., *Magn. Reson. Imaging* 1985, 3, 329.

[23] Komoroski, R.A., *Rubber Chem. Tech.* 1983, 5, 959.

[24] Vegvari, P.C., Hess, W.M., Chirico, V.E., *Rubber Chem. Tech.* 1978, 51, 817.

[25] Kadunce, R.J., Smith, R.W., *Int. Symp. for Testing and Failure Anal. Los Angeles, CA, November 1987 Abstracts* (ASM International, Metals Park, Ohio).

NMR IMAGING OF ELASTOMERS AND POROUS MEDIA

RICHARD A. KOMOROSKI AND SUBHENDRA N. SARKAR

University of Arkansas for Medical Sciences, Departments of
Radiology and Pathology, 4301 West Markham St., Little Rock, AR
72205.

ABSTRACT

NMR imaging has been applied to some elastomeric materials of industrial interest. The T_2 s of common elastomers, particularly after filling and curing, are sufficiently short that spin-echo sequences at submillisecond echo times cannot produce T_2 -independent images. The sensitivity to T_2 potentially makes spin echo imaging a good probe of elastomer blend composition, as demonstrated for a series of filled and cured *cis*-polybutadiene, styrene-butadiene rubber blends. The technique can be used to distinguish good and bad carbon black dispersion in actual tire tread samples. The configuration of polyester tire cord, voids, rubber layer boundaries, differences of molecular mobility and composition, and other inhomogeneities can be detected in end-product tire samples. The value of isotropic voxels at 80-100 μm and the effect of resolution relative to pore size are demonstrated on a model, H_2O -saturated porous glass disk of 200- μm average pore size. The feasibility of multinuclear NMR imaging for fluid-specific characterization of porous materials such as oil cores is demonstrated for ^7Li and ^{19}F .

INTRODUCTION

Nuclear magnetic resonance (NMR) imaging is being vigorously pursued as a nondestructive characterization tool for materials. The promise of measuring spin concentration, molecular mobility [via the spin-lattice (T_1) and spin-spin (T_2) relaxation times], and chemical structure (by largely unrealized localized spectroscopy techniques) at various locations within a sample has resulted in initial applications in a wide variety of nonmedical areas.^[1] Sizes have ranged from tree trunks of 25-cm diameter^[2] to "microscopic" studies on millimeter-sized objects at 50-100 μm resolution.^[3,4]

Because standard NMR imaging techniques are limited to observing molecularly mobile components, applications to date have concentrated on bulk elastomers^[5], solvent diffusion^[6], and liquids in porous inorganic materials such as ceramics and oil cores.^[7,8] Techniques are being developed for imaging of highly rigid materials^[9], which is the subject of other papers in this proceedings.

For standard NMR imaging techniques, the primary requirement for increased resolution is powerful gradients. For medical imaging, gradients typically never exceed 1 G/cm. Figure 1 shows plots of gradient strength G vs. acquisition time AT for various image resolutions. The significance of the acquisition time is that in echo imaging, it is limited by (and often equal to) the echo time TE. For materials, T_2 can be quite short, and hence TE or AT cannot be lengthened without

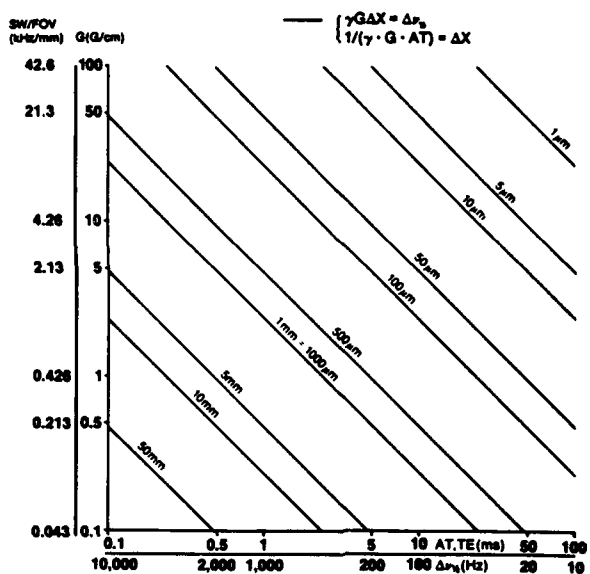


Figure 1. Plots of G and spectral width (SW)/field of view (FOV) versus AT (TE) or line width for various resolutions.



Figure 2. NMR image of a series of 2-mm sheets of cured, filled CB/SBR blends. Polymer compositions (CB:SBR) are from bottom: 100:0, 80:20, 60:40, 40:60, 20:80, 0:100.

loss of echo signal. Another consideration is the resonance line width of the material. The spread of frequencies caused by the gradient must be larger than the spread inherent in the line width. This relationship is also shown in Figure 1 for the limiting case where gradient spread equals the line width. Hence the relatively large line widths seen for materials also necessitate powerful gradients, typically 10 G/cm or larger.

In this report we explore applications of NMR imaging to direct analysis of bulk elastomeric materials of industrial interest and porous media. Current limitations and new directions of research are discussed.

EXPERIMENTAL METHODS

The ^1H NMR images were acquired at 200.1 MHz on a General Electric Omega CSI-4.7 system with Acustar shielded gradients and available bore size of 120 mm. The maximum gradient strength was 20 G/cm. Either a standard single-plane, spin-echo sequence with slice-selective 90 and 180° pulses [5] or a 3D volume imaging sequence was used. The 3D volume sequence employed a hard, initial 90° excitation pulse of 15-70 μs (depending on the coil) to excite spins in the entire object. Phase encoding was performed in the slice-select direction and one transverse direction, with frequency encoding in the remaining direction. For small objects at higher resolution, a commercial, single-turn surface coil of 2-cm diameter was used for both excitation and detection. For larger objects and oil cores, a 6.0-cm diameter, home-made birdcage coil was used. Lithium-7 and ^{19}F images were acquired on the same instrument at 77.8 and 188.2 MHz, respectively. For ^7Li a 5.5-cm birdcage coil was used, whereas for ^{19}F a 2-cm, single-turn surface coil provided both excitation and detection.

Carbon-13 NMR spectra were acquired at 75 MHz and 90°C on a General Electric GN-300 WB high resolution spectrometer with proton scalar decoupling in spinning 10-mm NMR tubes.

RESULTS AND DISCUSSION

Elastomer Composition and T_2

We previously demonstrated that standard spin-echo techniques at TEs of 10 ms or greater could be used successfully to image favorable cases of cured elastomers. [5] Many common elastomers have T_2 's of 0.5-2 ms [10], making it necessary to use short TE sequences such as 3D volume imaging described above to capture sufficient signal intensity. We have imaged elastomeric materials at TEs as low as 500 μs . However, even at submillisecond TEs it is not possible to obtain images for typical pure elastomers without T_2 affecting signal intensity and contrast. Of course, the filling and curing that impart the desired mechanical properties further reduce T_2 from that of the pure elastomer.

Figure 2 shows an NMR image (200 x 200 x 500 μm voxels) from a 3D volume dataset for a phantom composed of 2-mm sheets of a common series of cured, carbon-black filled *cis*-polybutadiene, emulsion styrene-butadiene rubber (CB/SBR) blends. Although all the blends have approximately the same hydrogen content, image intensity varies dramatically among the

blends. As the SBR ($T_g = -70^\circ\text{C}$) content increases relative to CB ($T_g = -102^\circ\text{C}$), T_2 decreases and image intensity decreases at a TE of 1.2 ms, as in Figure 2, or even at a TE of 500 μs . This is also apparent from the image profile on the right in Figure 2.

Conversely, the results in Figure 2 illustrate that NMR imaging can be a sensitive measure of polymer blend composition in well defined situations. Differences as small as 10% may be detectable. Such an approach may provide a substitute for localized spectroscopy techniques, which currently seem of limited use for complex, short T_2 materials.

Tire Materials

Inhomogeneities in elastomers have been imaged directly [5,11] and by solvent swelling.[12] Detection of an ^1H -rich, relatively mobile swelling agent in a polymeric material produces images of high quality. However, spatially dependent differential swelling and dimensional changes make interpretation of such images problematic. Direct imaging at short TE of cured, filled elastomer blends such as tire sections is preferred and can be highly informative. Figure 3 shows NMR images (250 x 250 x 500 μm voxels, TE = 4 ms) of actual finished tire tread sections. The section in Figure 3A was from a tire tread with a good, homogeneous carbon black dispersion, whereas that in Figure 3B had a poor dispersion. The samples appeared visually similar. The images are dramatically different and reflect the degree of filler dispersion. The good dispersion image has a relatively even distribution of NMR intensity, whereas the poor dispersion image appears spotty and highly heterogeneous, even in higher resolution (200 3 μm^3) images of thinner slices throughout the sample. Tread grooves are seen in both images. Numerous local inhomogeneities of a lesser nature are also seen in Figure 3A. We have routinely observed such inhomogeneities in a variety of elastomer compounds, both cured and uncured.

Figure 4 is an NMR image (100 x 100 x 200 μm voxels at TE of 2 ms) of a transverse section of a simple tire containing polyester fiber tire cord. The arrangement and shape of the cord fibers, as well as numerous irregularities, are clearly visible. The laminate structure of the section is well defined. This consists of a 2-mm wide layer on the left which corresponds to the tread. This is bonded to the 5.5 mm layer containing the cords in the center, with a barely visible 2-mm layer on the right. The right-hand layer is the inner liner of the tire, and it appears to consist of two layers from the image and profile although visually this is not apparent.

Carbon-13 NMR spectra of samples taken from the left (closest to the cord) and right sides of the right hand layer show the elastomeric components of these to consist of an isoprene rubber, butyl rubber blend, and probably pure butyl rubber, respectively. This is not unexpected as butyl rubber is commonly used as an air barrier on the inner surface of tubeless tires. It also explains the difficulty in observing this layer by NMR imaging. Butyl rubber is very difficult to image by standard techniques [5] because of its uncharacteristically short T_2 , which is a consequence of reduced chain segmental mobility.[13] The addition of isoprene rubber to butyl would increase segmental mobility in the blend, making that layer more

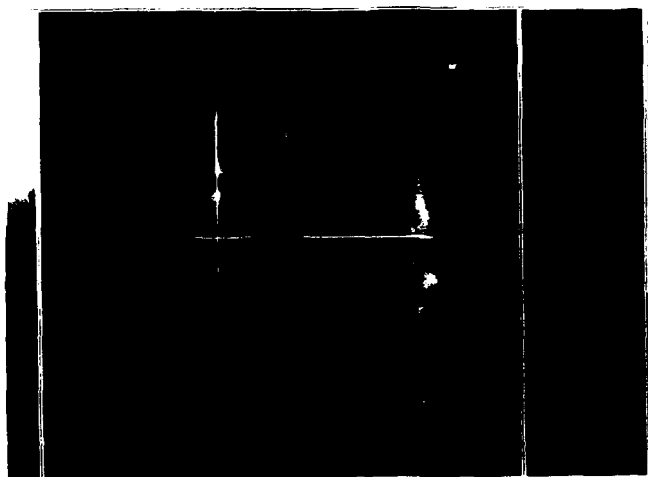
A**B**

Figure 3. NMR images of actual finished tire tread sections. Tread grooves are seen in each image. A) Good dispersion of carbon black; B) bad dispersion of carbon black. TE = 4 ms. 250 x 250 x 500 mm voxels.

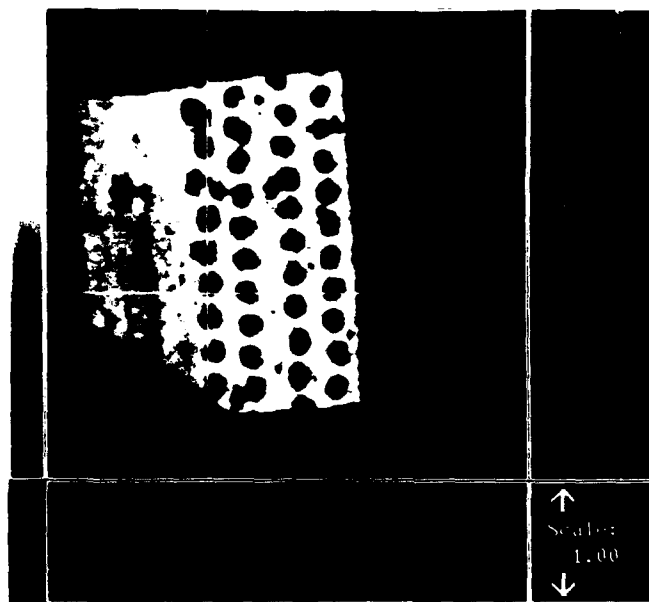


Figure 4. NMR image (slice #9 of 16, 100 x 100 x 200 μm voxels, TE = 2 ms) of a tire section with polyester cord belts. The FOV is 12.8 x 12.8 mm. One two-component layer, due to the inner liner of the tire, is barely visible on the right side of the image.

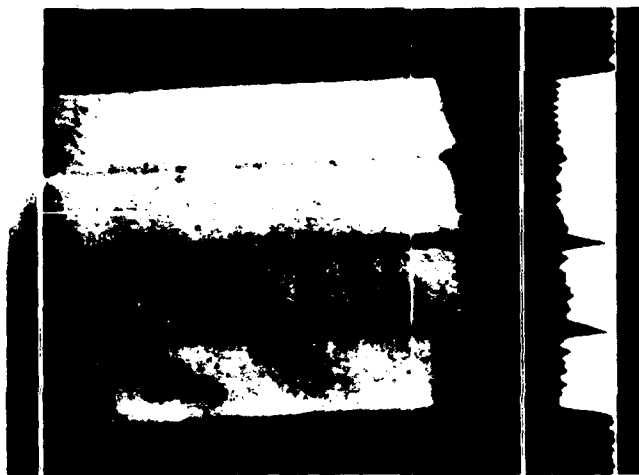


Figure 5. Image (80 x 80 x 500 μm voxels, TE = 4.3 ms) of 4 cured, filled 2-mm CB sheets. The bottom three sheets are separated by glass spacers of 180- μm thickness. The top two sheets have no spacer.

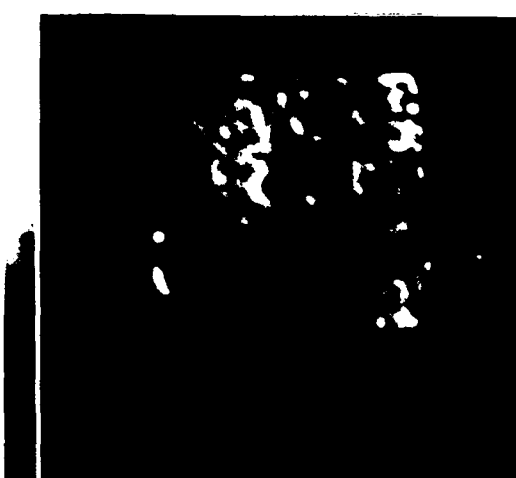
visible than pure butyl in the image. This sample has a material feature that might have gone undetected without NMR imaging.

The relatively large feature in the left layer consists of a low-intensity region surrounded by three spots of higher intensity. This is apparently a solid particle or agglomerate of carbon black or other material. The bright spots are probably magnetic susceptibility artifacts associated with the particle, and appearing along the readout (horizontal) direction, as was confirmed by imaging the object in several orientations. We see such artifacts routinely in carbon-black-filled rubbers, both cured and uncured.

In the image in Figure 4 the rubber layer boundaries are well defined because the layers have different combinations of T_2 and mobile hydrogen densities. For layers of identical material, detection of layer boundaries may be less straightforward. We previously demonstrated that in model elastomers boundaries beyond the image resolution can be detected by reduction of voxel intensity at that point.[5] Under the relatively poor resolution and long TE conditions of the previously published images [5], it was not clear if such sub-resolution boundary detection was from depletion of hydrogen content, lower T_2 at the surface, or both. Figure 5 shows higher resolution (80 x 80 x 500 μm) images of the same sheets as before [5] with 180- μm spacers at two boundaries and with no spacer at the third boundary. The sheets were firmly pressed together and secured for this experiment to eliminate the possibility of casual air space between the sheets. As expected, the spacers were well resolved. However, the boundary without spacer was also detected. Examination of image profiles at higher resolution suggests that this arises (under these conditions) from a slightly reduced amount of NMR visible rubber in the 200- μm region at the surface of the sheet. Hahn spin-echo experiments between 3 and 10 ms measure essentially the same T_2 at the surface as in the bulk rubber.[10] These results suggest that laminate boundaries may be more readily detectable for separately cured sheets than for uncured or co-cured materials.

Model Porous Materials

To date, most NMR imaging of materials has been with highly anisotropic voxels and poor resolution perpendicular to the slice. The advantage of isotropic voxels for visualizing complex 3D structures and minimizing confusing partial volume effects has been recognized.[14] Although 3D volume imaging may ultimately be the method of choice for obtaining isotropic voxels, it is possible to use the single-slice technique at moderately good resolution. Figures 6A-C show images of a 7 x 7 mm piece of a water-saturated, porous glass disk (35% porosity, pore size 170-220 μm) at three different isotropic resolutions—less than, at, and greater than the nominal pore size. As expected, the images are dramatically different and, in particular, display how features in the low resolution image arise from different planes in the slice. In the 100- μm isotropic-voxel image, there are a few small and intense spots whose size is about 190 $\mu\text{m} \times$ 190 μm in plane and are either single pores or collections of smaller pores. Longer spots may be pores connected in plane. Small and weak spots may be from

A**B**

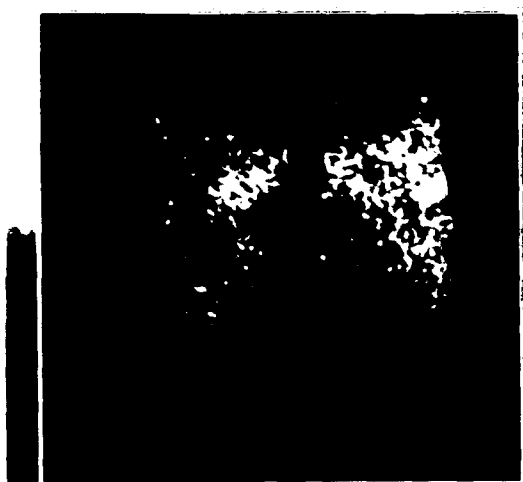
C**D**

Figure 6. NMR images of a 7 x 7 mm portion of a sintered glass disk of 35% porosity and nominal pore size 170-220 μm at three isotropic resolutions: A) 100 μm ; B) 200 μm ; and C) 400 μm ; D) 100 x 100 x 2000 μm voxels.

pores of about 100- μm size or less and fully included in the slice, or from larger pores partially cut by the 100- μm slice. For the 200- μm and 400- μm isotropic resolution images (Figures 6B and 6C, respectively), a few intense spots become larger as the resolution becomes coarser. Some of the spots remain bright, implying perhaps collections of water-filled pores from various planes. Images of other porous glass disks of 5-50 μm pore size suggest that the image appearance is dominated by the large-pore tail of a pore size distribution.[10]

The higher-resolution appearance of Figure 6A is retained to some extent in Figure 6D, an image with 100 \times 100 \times 2000 μm voxels, even though features from the equivalent of twenty 100- μm slice thicknesses contribute to the latter image. This arises from the fact that the majority of the object volume in this case is occupied by glass or air, and hence many of the anisotropic voxels have little or no signal. For porous materials of low-to-medium porosity and relatively large pore size, thick slices may provide more useful information than for relatively homogeneous materials such as polymers.

The results of Figure 6 also demonstrate that obtaining isotropic voxels at high resolution will not exact too severe a penalty in S/N ratio for porous materials. Although the voxel volume in the 100- μm image is 1/64th that of the 400- μm image, it took only 16 times (4x S/N penalty) as long to obtain the 100- μm image. This arises from the "dilution" of the signal in a single voxel by glass as the resolution becomes coarser.

Multinuclear Imaging of Porous Materials

NMR imaging is being used increasingly to study the fluid distribution in oil cores.[8,15] Since such imaging is usually concerned with the distribution of two or more fluids such as oil and water in the rock, methods for separate observation of the components must be developed. For cases where individual resonances can be resolved for the oil and water components, we have used a radiofrequency presaturation pulse and dephasing gradient to produce component-selective images.[15] When resonance lines are broad and the individual components cannot be resolved, a multinuclear approach is necessary. Edelstein et al. [8] have used the ^1H and ^{13}C isotopes to analyze for the amounts of water and oil in whole cores. We have indirectly imaged a third fluid (isopropanol as a model miscible injectant) in a core by profiling the disappearance of signal in the ^1H NMR image when the third fluid is deuterated.[15]

Direct multinuclear imaging of isotopes confined to a single phase should provide unambiguous separation of two or more components in model systems. Possible nuclei include ^{19}F (fluoride or fluorinated organics), ^{13}C (organics, CO_2), ^{23}Na (brine), ^7Li (brine), ^2D (D_2O or deuterated organics), and ^{17}O (H_2O), in addition to ^1H . As an example, Figure 7A shows the ^7Li NMR image of a Li brine in a model porous glass filter disk of nominal pore size of 200 μm . The ^7Li isotope is favorable for such studies, with a sensitivity about 27% that of ^1H , relatively narrow lines, T_2 s of 10-500 ms, and T_1 s of 0.5-4 s in motionally restricted systems. Figure 7A shows that a resolution on the order of 1 \times 1 \times 5 mm^3 can be expected. Figure 7B shows a comparable image for ^{19}F of 50% hexafluorobenzene in porous glass taken using a surface coil. We have obtained preliminary ^7Li and ^{19}F images on actual oil cores.

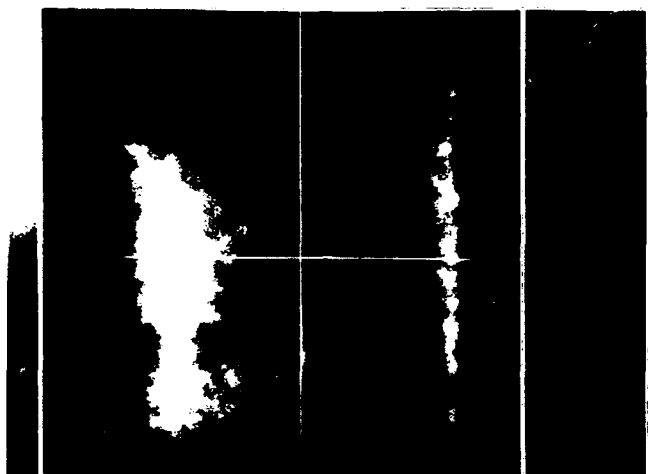
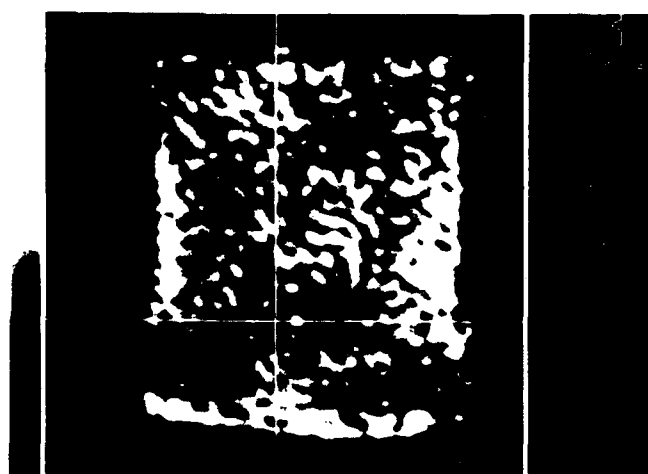
A**B**

Figure 7. A) ^{7}Li NMR image of a portion of a sintered glass disk (35% porosity, 170-220 μm pore size) with 2 M LiCl . (1 \times 1 \times 5 mm voxels; TE = 2 ms; FOV, 64 \times 64 mm); B) ^{19}F NMR image of a sintered glass disk (40% porosity, 4-5.5 μm pore size) with 50% hexafluorobenzene. (200 \times 200 \times 2000 μm voxels; TE = 2.8 ms; FOV, 12.8 \times 12.8 mm)

Resolution better than ^7Li can be expected for ^{19}F in comparable cases (Figure 7B). The ^{19}F T_2 may be short, on the order of 2 to 10 ms. For both ^7Li and ^{19}F it will be necessary to use short TE sequences such as whole-core 3D volume imaging.

ACKNOWLEDGEMENTS

We thank Ken Schur of the BF Goodrich Company for providing the elastomer and tire samples, and Annadell Fowler for running the ^{13}C NMR spectra. This work was supported in part by grant AFOSR-89-0418 from the Air Force Office of Scientific Research.

REFERENCES

1. J.M. Listerud, S.W. Sinton, and G.P. Drobny, *Anal. Chem.* **61**, 23A (1989).
2. S.J. Chang, J.R. Olson, and P.C. Wang, *For. Prod. J.* **29**, 43 (1989).
3. C.F. Jenner, Y. Xia, C.D. Eccles, and P.T. Callaghan, *Nature* **336**, 399 (1988).
4. W. Kuhn, *Angew. Chem. Int. Ed. Eng.* **29**, 1 (1990).
5. C. Chang and R.A. Komoroski, *Macromolecules* **22**, 600 (1989).
6. L.A. Weissenberger and J.L. Koenig, *Appl. Spectrosc.* **43**, 1117 (1989).
7. L. Garrido, J.L. Ackerman, and W.A. Ellingson, *J. Magn. Reson.* **88**, 340 (1990).
8. W.A. Edelstein, H.J. Vinegar, P.N. Tutunjian, P.B. Roemer, and O.M. Mueller, *SPE Paper 18272*, 63rd Annual Technical Conference and Exhibition, Houston, TX, Oct. 2-5, 1988.
9. D.G. Cory, J.B. Miller, R. Turner, and A.N. Garroway, *Mol. Phys.* **70**, 331 (1990).
10. S.N. Sarkar and R.A. Komoroski, unpublished results.
11. A.G. Webb, P. Jezzard, L.D. Hall, and S. Ng, *Polym. Commun.* **30**, 363 (1989).
12. R.S. Clough and J.L. Koenig, *J. Polym. Sci. Polym. Lett.* **27**, 451 (1989).
13. R.A. Komoroski and L. Mandelkern, *J. Polym. Sci. Polym. Symp.* **54**, 201 (1976).
14. X. Zhou, C.S. Potter, P.C. Lauterbur, and B. Voth, *Abstracts, Eighth Annual Meeting, Soc. Magn. Reson. Med.*, 286 (1989).
15. J.J. Dechter, R.A. Komoroski, and S. Ramaprasad, *Proc. Soc. Core Analysts*, paper #8903, 1989.

NMR Imaging of Morphology, Defects, and Composition of Tire Composites and Model Elastomer Blends

Subhendra N. Sarkar and Richard A. Komoroski*

Departments of Radiology and Pathology, University of Arkansas for Medical Sciences,
4301 West Markham Street, Little Rock, Arkansas 72205

Received July 11, 1991

ABSTRACT: Multiple-slice, three-dimensional (3D) ¹H NMR imaging at medium resolution (100–200 μ m) and short echo times (0.5–2 ms) has been used to visualize the elastomeric components of several tire sections. The various rubber layers and cords were readily distinguished for a non-steel-belted tire section at 200- μ m resolution, presumably based on T_2 differences among the different components. Carbon-13 magic angle spinning NMR of samples from each layer provided elastomer composition, which supported the origin of the intensity differences seen by NMR imaging. The ability to detect small differences of composition in actual tires was confirmed by imaging well-characterized diblends of *cis*-polybutadiene (BR) and styrene-butadiene rubbers (SBR). From T_2 -weighted images or from the total intensity profiles, a 20% difference in blend composition was distinguished. Experimental tire tread sections with good and poor carbon black dispersions produced substantially different images at 150- μ m in-plane resolution. Artifactual intensity patterns from bulk magnetic susceptibility differences between certain defects and the elastomer matrix were observed in some of the samples and may be useful for defect identification.

Introduction

Nuclear magnetic resonance (NMR) imaging is a promising tool for nondestructive mapping of spatial structures in materials.¹ Currently, only relatively concentrated constituents with high molecular mobility are routinely imageable. This includes low-molecular-weight diffusants in polymers^{2,3} or porous materials,^{4,5} polymeric binders in green ceramics,⁶ and elastomeric materials well above their T_g .^{7–10}

A major focus of NMR imaging research is currently on difficult-to-image rigid materials. Glassy or crystalline materials have very short transverse spin relaxation times (T_2) and large line widths and require experimentally demanding line-narrowing methods in conjunction with imaging techniques.^{11,12} Magic angle spinning (MAS) combined with imaging techniques¹³ is possible but seems impractical for large or irregular industrial samples. The use of mobile penetrants in rigid materials or rubbers can improve the ability to obtain images. However, this may create differential swelling and local dimensional changes that make interpretation of such images problematic.

Image-guided localized ¹H spectroscopy¹⁴ can potentially provide information on molecular composition for regions of several cubic millimeters in samples of high molecular mobility. However, in materials ¹H lines are broad and unresolved, making localized ¹H spectroscopy an unattractive choice.¹⁵

To date no study has appeared using NMR imaging to detect variations in composition of tire composites and elastomeric blends. Such materials have moderately narrow NMR lines (300–1000 Hz) due to polymer chain segmental motions,¹⁵ with ¹H T_{2s} typically in the range of 0.5–5 ms which is beyond the range of echo times (TE) available on medical imagers.⁷

One approach to characterize materials of this type is to stretch the current limitations of medical NMR imaging by employing strong, actively shielded gradients capable of fast switching (50–100 μ s) and submillisecond TE and intermediate-size magnet bores (10–25 cm) capable of accommodating a wider range of samples than standard high-resolution NMR systems. We have used a modified,

three-dimensional (3D) volume imaging approach¹⁶ to achieve short TE (<1 ms), practical image resolutions (100–200 μ m) close to the predicted limits for elastomer line widths,⁷ and contiguous multislice images of whole samples in a few minutes to a few hours. This work emphasizes development of NMR imaging as a nondestructive mapping technique sensitive to blend composition, filler dispersion, curing, and defects in filled, cured elastomers as a continuation of previous work.^{7,8,17}

We report here NMR images of several tire sections which demonstrate visualization of composite elastomeric layers of varying composition, tire cords, and differences in dispersion of carbon black in finished tire tread. Images of model diblends yield an estimate of the sensitivity of the technique to elastomer compositional changes. Finally, abrupt changes in magnetic susceptibility at defect interfaces can create shape and intensity artifacts in NMR images.^{18,19} We report the observation of such artifacts in filled elastomers.

Experimental Section

Samples. For imaging studies, sections about 10 mm \times 10 mm square and 4 mm thick from three finished tires were taken. One sample consisted of a transverse cross section of a small, non-steel-belted bias-ply tire. In addition, tread samples were cut from sections of two experimental steel-belted, radial automobile tires specially prepared with treads having good and poor dispersion of carbon black, as measured by the AMEDA (Automatic Microscope Electronic Data Accumulator) technique.²⁰

In addition, a set of eight well-characterized elastomer samples was studied. The set consisted of uncured, unfilled *cis*-polybutadiene (*cis*-BR) and emulsion styrene-butadiene (SBR; 23.5% styrene) rubbers and six 2-mm-thick sheets of cured (at 160 °C for 20–25 min) and filled (60 phr carbon black) diblends with *cis*-BR/SBR compositions of 100:0, 80:20, 60:40, 40:60, 20:80, and 0:100 by weight. Other initial components before cure included 15% processing oil, 0.9% stearic acid, 2% antioxidant, 2% tackifier, 2% antioxidant, 3% zinc oxide, 1.7% sulfur, and 1.5% accelerator. The processing oil is largely volatilized in the curing process. Images were obtained for the blend sheets cut to a size of 2 \times 4 \times 10 mm³. The 10-mm-long and 2-mm-thick edges were laid with fixed spacing between the individual sheets in the plane (xz plane of the magnet) by means of glass spacers.

Finally, a phantom was prepared with "defects" of known geometry and bulk magnetic susceptibility differences by em-

* To whom all correspondence should be addressed.

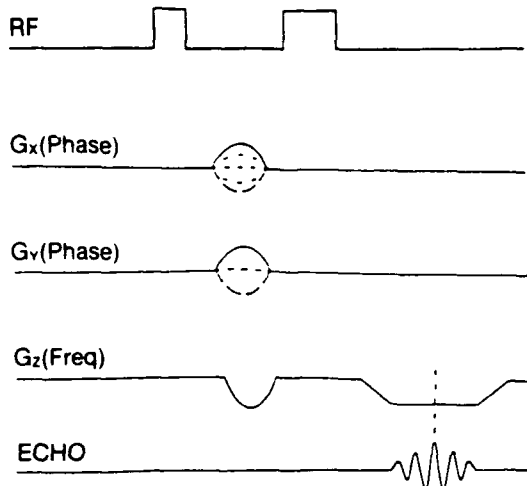


Figure 1. Schematic diagram of the 3D whole volume imaging sequence used to acquire images in the text. Slice selection was done by phase encoding in the *y* direction.

bedding an air-filled glass capillary tube, a carbon-black-filled glass capillary, and a graphite pencil tip in a matrix of commercial vegetable shortening (Crisco, Proctor and Gamble Co.) contained in a glass vial. Carbon black was also mixed directly into a region of the vegetable shortening.

3D Imaging at 4.7 T. A General Electric Omega CSI 4.7-T system with Acustar shielded gradients and a maximum gradient strength of 20 G/cm in a 120-mm magnet bore was used to image ^1H at 200.1 MHz. Samples were imaged with a single-turn, 2-cm ^1H surface coil for both excitation and detection. The positioning and size of the samples relative to the surface coil were such that the radio-frequency field inhomogeneities over the volume of the sample examined were minimal.

The 3D volume imaging pulse sequence shown in Figure 1 was employed for obtaining contiguous multislices to cover the entire volume of the samples. In this sequence, a rectangular 90° pulse of 17–20- μs duration was applied to excite the entire sample. Phase encoding was done by stepping gradients (one-lobe sinusoidal, 20 G/cm, 250–300- μs duration) 128 and 16 times, respectively, in the *x* and *y* directions. The frequency encoding gradient (*z* direction) was about 10 G/cm. A maximum digitizing rate of 200 kHz (128 points) was used to minimize the acquisition time. Crusher gradients were not required. The echo times were 0.5–2 ms for in-plane resolutions from 400 \times 400 to 100 \times 100 μm^2 . Slice thicknesses were typically 0.2–0.5 mm. The sum of the intensities along the phase-encode direction for the diblend sheet sample was obtained by turning off the phase-encode gradients at TEs ranging from 0.5 to 6 ms.

The spin-lattice relaxation times (T_1) of the broad ^1H peak for each of the tire sections, for the six blend sheets together, and for each of the sheets separately were measured by the inversion-recovery method and the T_2 values by the Hahn spin-echo technique at 4.7 T.

Spectroscopy at 7.05 T. Mobile ^1H contents for all samples were determined by integrating the peak intensities of ^1H spectra at 300.5 MHz (pw 6.8 μs , tip angle 90°, single scan) on a General Electric GN-300WB spectrometer at 19 °C in 5-mm NMR tubes. The values were normalized with respect to that of cured 100:0 *cis*-BR/SBR. The ^{13}C MAS NMR spectra were obtained at 75.57 MHz (pw 7.8 μs , tip angle 38°, repetition time 2 s) from about 0.5 g of finely cut rubber pieces from various layers of the non-steel-belted tire in a Chemagnetics MAS accessory employing 9-mm rotors at about a 400-Hz spinning rate with pulse-modulated low-power ^1H decoupling at 20 °C. No serious attempt was made to quantitate the ^{13}C MAS spectra.

Results and Discussion

The details of the modified 3D imaging sequence¹⁶ have been described in the Experimental Section. Advantages of this sequence are (1) short echo times, (2) nonoverlapping, contiguous slices of the entire sample, and (3) a

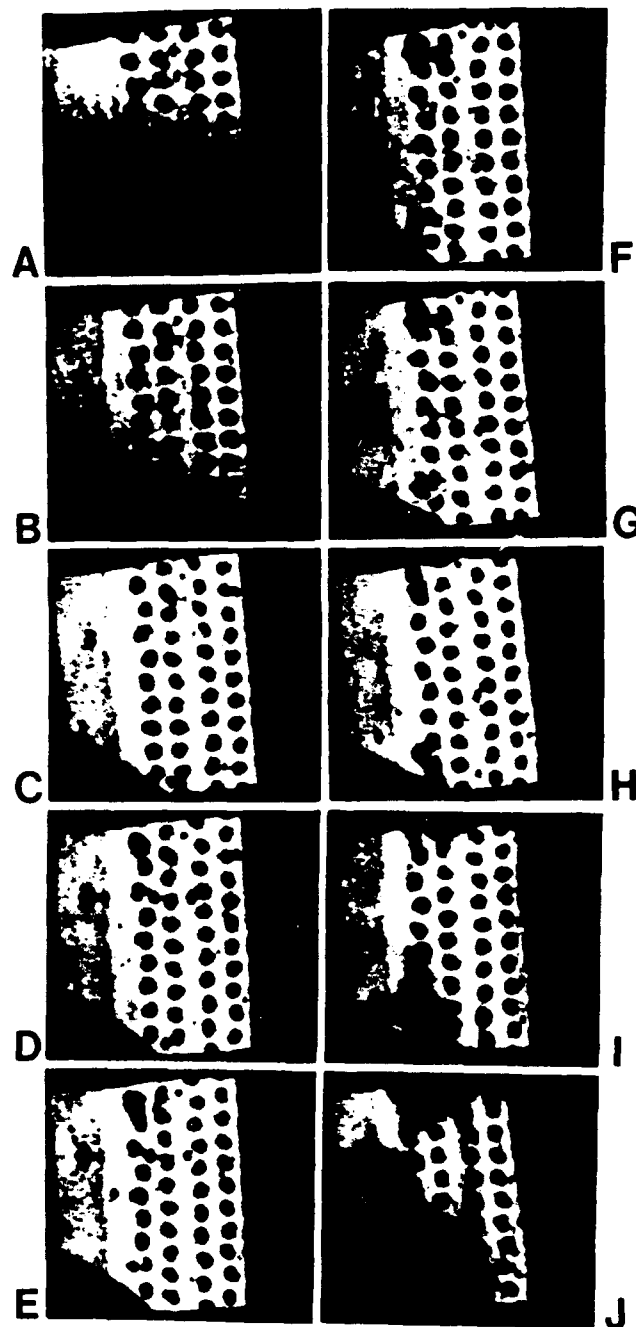


Figure 2. Ten image slices (200 μm thick; FOV 9 mm) (A–J) of 100- μm in-plane resolution covering the entire volume of a cross section of a non-steel-belted tire. TE, 1.9 ms; TR, 1 s; total time, 2 h; data size, 128 \times 128 \times 16. Here slice A was closest to the radio-frequency coil, and the image intensity was manually adjusted for uniformity among the slices.

large excitation bandwidth resulting from narrow radio-frequency pulses. The major disadvantage for imaging whole volumes of large samples is that high isotropic resolution requires long data acquisition times and processing of large data sets. Crusher gradients are commonly inserted into imaging pulse sequences to destroy residual, unwanted transverse magnetization from pulse imperfections that can produce image artifacts. We found such crusher gradients to be unnecessary here, presumably because such residual transverse magnetization is short-lived for the short- T_2 samples examined.

3D NMR Imaging and ^{13}C NMR of a Tire Section. Figure 2 shows 10 (from a set of 16) contiguous transverse slices, each 200 μm thick, of a 3D NMR image at a TE of 1.9 ms covering the entire volume of the non-steel-belted

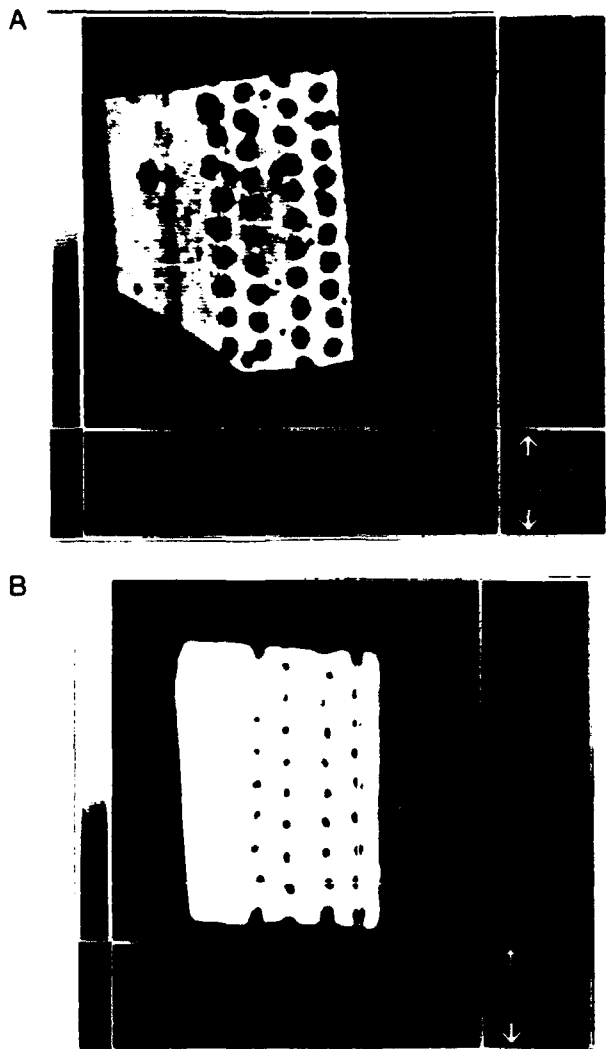


Figure 3. (A) Expansion of the image in Figure 2D. (B) 500- μ m slice (TE, 750 μ s) centered at the same plane as that of Figure 2D at 200- μ m in-plane resolution with the intensity burned-in to highlight the presence of two weak layers on the right.

tire cross section. The tread is to the left and the interior portion of the tire to the right. At the in-plane resolution of 100 μ m, the tread layer at the left can be distinguished from the second region of higher intensity containing embedded rigid fibers appearing as dark spots in each slice. The layer boundary as well as the fiber-rubber interfaces is well-defined. In the T_2 -weighted images, the fibers yield no signal because of very short T_2 associated with the absence of substantial molecular motion. Visual examination of the tire cross section and the cord placement reveals that a region to the right of the cords is not appearing in Figure 2. A 2-mm-thick layer, which visually appears no different from the leftmost layer, is barely visible on the right. Numerous other defects, presumably voids, chunks of carbon black or other material, and broken or misaligned fibers are also present in these images. The 3D structure of the various defects is well-defined in this set of contiguous, reasonably thin slices. Some of the defects display a characteristic arrowhead pattern¹⁹ of bright spots pointing along the frequency encode direction. This pattern results from magnetic susceptibility differences between the defect and the surrounding matrix and is described in more detail later.

Figure 3A shows the same slice as in Figure 2D, expanded to reveal more details. The rightmost layer mentioned above is barely visible in the image and profile (at the

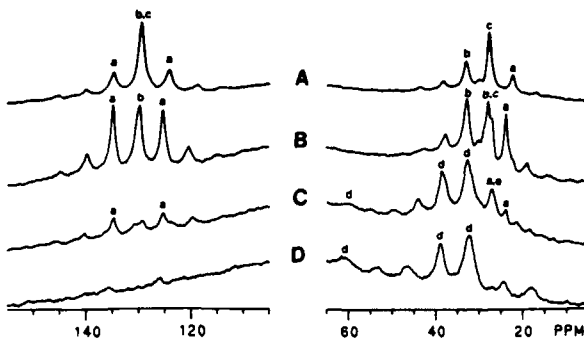


Figure 4. ^{13}C scalar-decoupled MAS spectra at 75.57 MHz and a spin rate of about 400 Hz. (A) Sample from the outermost layer (tread) of a tubeless tire. (B) Sample from the middle region including rigid fibers. (C) Sample from the left of the two rightmost inner layers. (D) Sample from the innermost layer on the right. Peaks are from NR (a), cis-BR (b), SBR (c), butyl rubber (d), and spinning sideband (e).

bottom in Figure 3A), which are suggestive of two layers in this region. Figure 3B is an image of a 500- μ m slice centered at the same plane as that of Figure 2D. Here the TE has been shortened to 750 μ s, with the accompanying loss in resolution (200 \times 200 \times 500 μ m). The image has been burned-in to clearly show the presence of the rightmost layer, which is more clearly defined as two layers in the profile at the bottom. The combination of shorter TE and coarser resolution has enhanced the visibility of this feature. The result in Figure 3 demonstrates the advantage of submillisecond TE for observing structures in spin-echo images of elastomeric products. The two-layer nature of the rightmost region was not visually apparent and is a feature detectable perhaps only by NMR imaging.

Intensity differences in T_2 -weighted NMR images of previously uncharacterized finished products, such as the tire section shown here, may arise from several sources, including differences in rubber content, composition, filler, and cure for example. A complete chemical and morphological characterization of the tire section in question is beyond the scope of this work. However, a limited analysis of the elastomer composition of the various layers has been performed to provide a likely rationalization of the intensity variations among layers in Figures 2 and 3.

Figure 4 shows four scalar-decoupled ^{13}C MAS spectra at 75.57 MHz corresponding to sample A, the outermost layer (tread), sample B, the middle layer containing fibers, sample C, the layer immediately adjacent to B on the right, and sample D, the interior layer (closest to the enclosed air in a tubeless tire). These are ordered from left to right in Figures 2 and 3. The major peaks in all four spectra can tentatively be identified by comparison to high-resolution ^{13}C NMR spectra of common elastomers and blends.²¹ Assignments are given in the caption to Figure 4. Peaks not assigned are spinning sidebands of the major resonances or unidentified minor structures. Figure 4D corresponds to primarily butyl rubber²¹ (peaks marked d). Figure 4C shows the presence of a small amount of cis-polyisoprene or natural rubber (NR; peaks marked a) blended with butyl rubber. A spinning sideband (e), identified by varying the spin rate, overlaps one of the NR peaks. Spectra A and B in Figure 4 correspond to NR/cis-BR/SBR blends (peaks indicated by a-c, respectively) in the ratios of roughly 20:10:70 and 40:10:50, respectively. There is substantial ambiguity in the cis-BR/SBR ratios due to overlap of butadiene peaks.²¹

The tread layer has a lower intensity than the middle layer presumably due to its relatively higher amount of SBR and lower amount of NR. The innermost double

Table I
NMR Relaxation Times, Relative ^1H Contents, and
Linewidths of Actual and Experimental Tire Tread
Sections

tire sample	rel ^1H content	line width, Hz	T_1 , ms	T_2 , μs
bias-ply tire section		1850	410	<100, a 950
exptl tread, poor dispersion of carbon black	0.85	2600	450 (60%), 1000 (40%), 630	
exptl tread, good dispersion of carbon black	1.00	1400	380	1100

^a Minor component of T_2 responsible for 10% of the total intensity.

layer of greatly reduced intensity on the NMR images contains primarily butyl rubber. Butyl rubber is commonly used as an air barrier on the inner surface of tubeless tires. Although the T_g of polyisobutylene (and butyl rubber) is -70°C , its polymer chain segmental mobility is substantially restricted relative to elastomers of similar T_g , as has been demonstrated previously by ^{13}C spin relaxation measurements.²² Thus, with a shorter ^1H T_2 (<0.1 ms) than other common elastomers, butyl rubber is more difficult to detect in NMR images. The addition of some *cis*-polyisoprene rubber (natural or synthetic) would increase the ^1H T_2 of that layer, making it slightly more intense on the NMR image. The subtle difference in composition in the butyl-rubber-containing portion of this cross section is the type of feature that may only be discernable by NMR imaging, through its sensitivity to molecular composition via the dependence of spin relaxation on molecular mobility.

The image-guided destructive analysis by ^{13}C MAS NMR can offer further information supporting the non-destructive and quick observation available through NMR imaging. Bulk spectral or spin relaxation measurements obviously cannot provide the spatial detail nondestructively. The detailed composite nature of the tire tread as a whole is completely obscured in the measured values of ^1H NMR relaxation parameters and line widths given in Table I.

NMR Imaging of *cis*-BR/SBR Model Diblends. Application of NMR imaging to nondestructive characterization of material composition, particularly for composite elastomer systems, may require some type of calibration curve from the images of simpler, well-characterized components which comprise the whole composite system. Imaging of *cis*-BR/SBR diblends of known composition can demonstrate such an approach for an important class of elastomeric composites.

Six model sheets of *cis*-BR/SBR have been studied in detail. Relaxation parameters and line widths for each of the sheets and for the combined stack of all sheets are given in Table II. The increase in T_1 values with increasing SBR content is slight. For each of the blend sheets there was a short T_1 component (not given here) contributing about 10% of the total intensity, perhaps due to bound polymer on carbon black particles. Similarly, the change in line width with increasing SBR content tells little about the blends.

On the other hand, T_2 decreases steadily and substantially with increasing SBR content, which is a consequence of the decreased low-frequency segmental mobility of SBR (T_g of SBR = -55°C ; T_g of *cis*-BR = -102°C). For each of the sheets there was a minor, long component of T_2 responsible for the residual intensity that permitted imaging at much longer TEs. The origin of this long component may be intrinsic nonexponentiality of the relaxation process or traces of residual processing oil.

Table II
NMR Relaxation Times, Line Widths, and Relative ^1H Contents of *cis*-BR, SBR, and the Model Diblends at 4.7 T

comprn (cured, filled <i>cis</i> -BR:SBR wt %)	rel ^1H content	approx line widths	T_1 , ms	T_2 , μs
pure <i>cis</i> -BR		150	330	1100, 4000 ^a
pure SBR		550	440	500, 6000 ^a
100:0	1.00	650	270	1000
80:20	1.07	600	300	880
60:40	1.02	650	320	730
40:60	1.01	750	330	620
20:80	1.00	820	370	500
0:100	0.92	980	440	50-150
six sheets together		1200	420	750

^a Minor component of T_2 responsible for 10% of the total intensity.

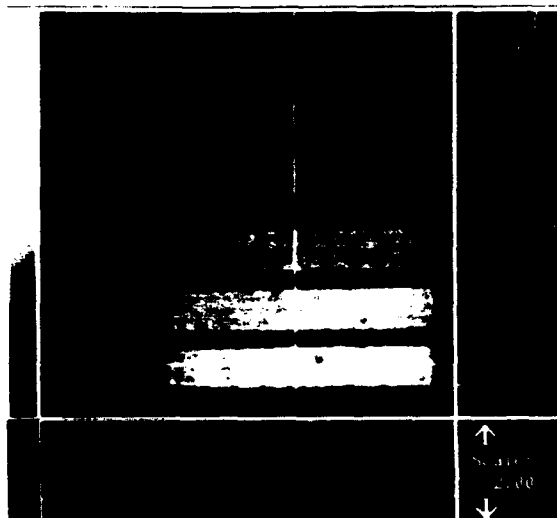


Figure 5. 500- μm slice from a 16-slice volume data set of six model diblend sheets of *cis*-BR/SBR with composition ratios 100:0, 80:20, 60:40, 40:60, 20:80, and 0:100 (bottom to top) at 200- μm in-plane resolution. TE, 1.1 ms; TR, 1 s; total time, 1 h.

The relative uniformity in ^1H density for these sheets (Table II) leaves the variation in T_2 as the prime cause of the image and profile intensity variations (see below). Under our pulsing conditions, the small range of T_1 of the sheets results in a very slight T_1 dependence, less than the variation in ^1H density. Note that measurement of any of the above NMR parameters on the stack of all six sheets tells very little about local composition variations in the composite.

Figure 5 shows a typical NMR image from a 16-slice, 3D dataset with $200 \times 200 \times 500 \mu\text{m}^3$ resolution for the six model *cis*-BR/SBR blend sheets at a TE of 1.1 ms. As the SBR content increases, the image intensity decreases as expected in regular fashion, which is also evident in the image profile on the right side. The results in Figure 5 demonstrate the ability of NMR imaging to exquisitely differentiate polymer blend compositions based on T_2 differences. The degree of differentiation depends on the variation in T_2 and the TE used. In this case the T_2 variation was at least 100 μs (10% of the TE used) between two adjacent sheets having a 20% difference in SBR content. Perhaps as little as a 10% variation in composition could be detected.

Figure 6 shows image profiles of the same stack of sheets at TE = 6, 1, and 0.5 ms. Clearly the use of a very short TE brings about a substantial improvement in our ability to detect the high-SBR-content sheets as it did for the butyl rubber layers of the tire section. However, as expected, we are not able to remove the effect of T_2 for

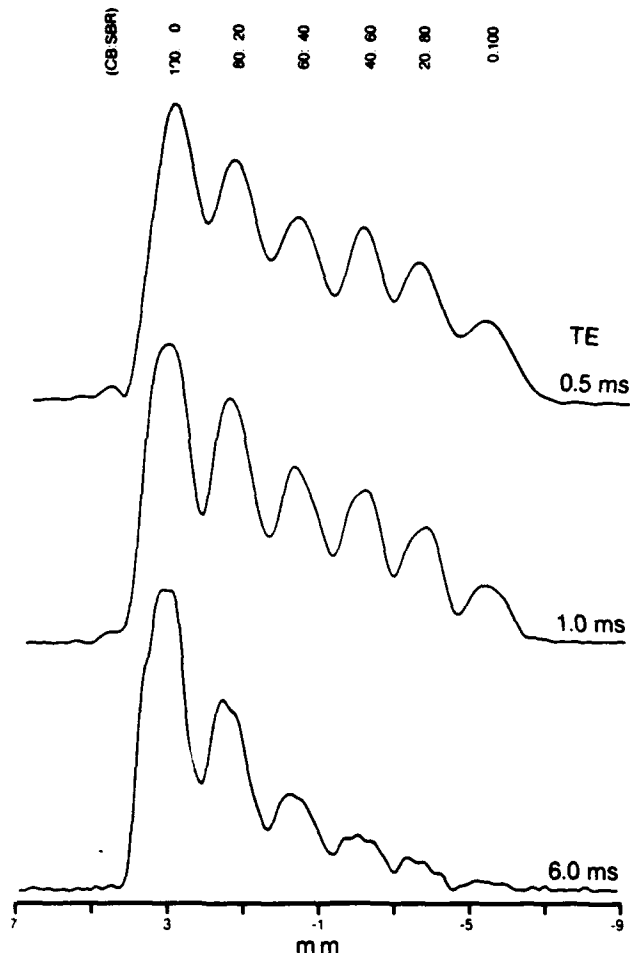


Figure 6. Summed intensity profiles from the cis-BR/SBR diblock sheets at TE 6, 1, and 0.5 ms. TR, 5 s; total time, 9 min.

these typical elastomers even at a TE of 0.5 ms. In a T_2 -independent profile, all six peaks would be of approximately equal intensity, as indicated by the results in the second column of Table II. Lowering the TE by a factor of 2–4 from 0.5 ms, as might be achieved by stronger gradients and a faster digitizer, will not radically improve our ability to image submillisecond T_2 materials such as butyl rubber and polychloroprene. At least a 10-fold reduction in TE is needed to obtain T_2 -independent images of most common cured and filled elastomers.

An alternative might be to employ line-narrowing pulse sequences used for rigid materials.^{11,12} However, it is not clear how effective line-narrowing sequences will be for elastomers, where the dipolar line width is strongly narrowed by chain segmental motion.¹⁵ In such a case, the characteristic frequency of the line-narrowing sequence must exceed the frequency of the segmental motion, which corresponds to a correlation time of about 10^{-8} s. In this case the only alternative is to increase the temperature of the sample.²³ Nevertheless, although T_2 -independent images cannot be obtained using the methods employed here, high-quality images sensitive to elastomer composition are possible.

Carbon Black Dispersion. The mechanical properties of a tire tread depend strongly on the degree of carbon black dispersion, among other things. A tire tread in which the carbon black is not well-dispersed displays inferior performance. Carbon black dispersion is typically measured at the surface by mechanical²⁴ or photometric techniques such as AMEDA.²⁰ There is no nondestructive way to characterize carbon black dispersion locally within a sample.

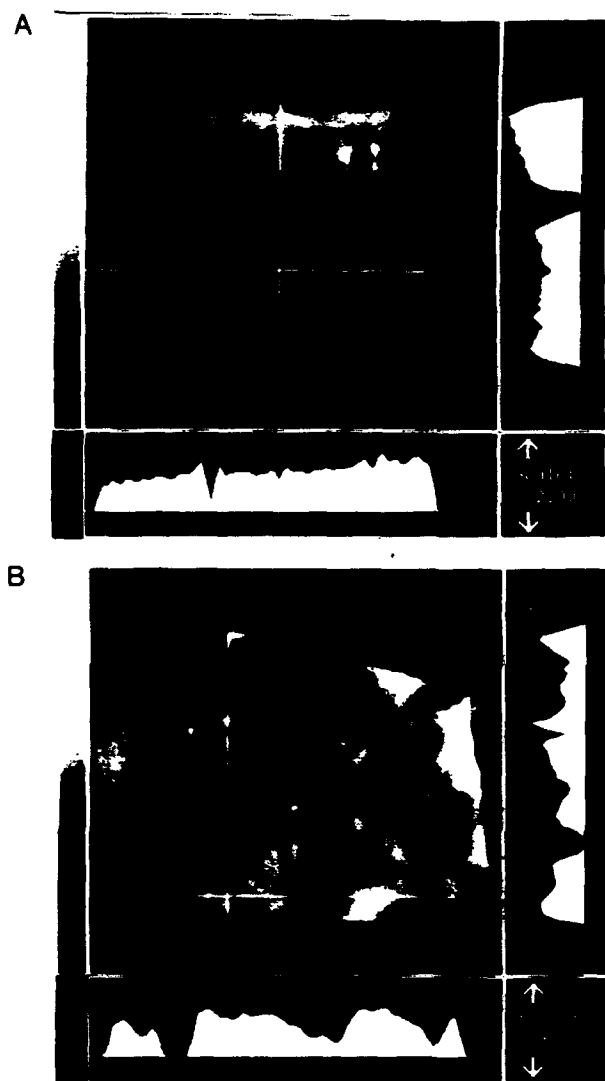


Figure 7. (A) Typical NMR image from an experimental tire tread with a good dispersion of carbon black at $150 \times 150 \times 350 \mu\text{m}^3$ resolution. Total time, 2 h. (B) NMR image of an experimental tire tread with a poor carbon black dispersion. TE, 1.3 ms; TR, 1 s for both.

Figure 7 shows typical images from two finished tire tread sections—one with good and the other with poor carbon black dispersion. Tread grooves are well-defined in both sections. The relatively even appearance in Figure 7A is consistent with well-dispersed carbon black, although the section is not defect-free. The image of Figure 7B displays a highly uneven appearance, consisting of regions of poor dispersion of several hundred microns diameter detectable at $150\text{-}\mu\text{m}$ in-plane resolution. The S/N ratio is generally lower for the tread with a poor dispersion, even though the imaging time was 5 times longer than that with the good dispersion. A substantial fraction of the NMR intensity is lost apparently due to the heterogeneous nature of the sample with a poor carbon black dispersion. Note that the T_2 measurements on the sections gave two values of T_2 for the poor dispersion sample, as compared to a single value of T_2 for the good dispersion sample (Table I). A fraction of polymer in the poor dispersion section has a substantially reduced T_2 , resulting in a signal loss at constant TE. This fraction may represent bound rubber. This is another example where the two results together provided more information than NMR imaging or relaxation parameters alone.

Magnetic Susceptibility Artifacts in NMR Images. In most of the images shown above, defects surrounded

by three bright spots in an arrowhead configuration appear in the frequency encode direction. Frequency shifts of a compartmentalized nucleus¹⁸ as well as the resulting field distortions¹⁹ due to interfacial magnetic susceptibility differences and compartment geometry can produce artifactual intensity patterns similar to those observed here. Such artifacts have been described in detail elsewhere.¹⁹ In addition to depending on the size and shape of the object, these distortions are proportional to the magnetic susceptibility difference across the interface and the static magnetic field strength and inversely proportional to the strength of the frequency encode gradient.¹⁹ Their direction reverses upon changing the gradient direction, which we have confirmed here in one case.

Since this pattern is common in the NMR images of carbon-black-filled elastomers, it is important to identify the source(s). Among the possibilities are voids, particles of metal or other foreign material, or agglomerates of carbon black. We suspect that the artifacts arise from relatively large particles of crystalline, graphitic carbon black ("coke") which are usually present in the unmixed carbon black and are produced in the carbon black manufacturing process.²⁵ The location and size of such particles are important in that they can serve as initial points for failure under stress or in service.²⁵

This undesirable component could result in a large magnetic susceptibility difference relative to the surrounding filled elastomer. As a crude test of this hypothesis, Figure 8A shows a typical volume image of a phantom consisting of a glass capillary filled with air (top right), another glass capillary filled with powdered carbon black (close to center), and a graphite pencil tip (lower center) embedded in a matrix of commercial vegetable shortening. Additional irregular air pockets are also visible. About a third of the total volume of this matrix at the top was mixed directly with about 1 g of powdered carbon black.

No prominent magnetic susceptibility artifacts are seen at any of the air pockets or either glass capillary. A prominent arrowhead artifact appears only at the graphite tip. Figure 8B shows the gradient-recalled-echo image of the same slice. In this sequence the read gradient polarity is reversed to refocus the spins, instead of a 180° pulse.⁷ Such images are generally sensitive to T_2^* , the time constant for decay of the free induction signal. Defects can appear magnified in such images if a magnetic susceptibility difference produces reduced T_2^* near the defect surface.⁷ Note that the arrowhead pattern is washed away and the feature from the pencil tip greatly enlarged. Most of the other defects undergo no or minimal enlargement. No evidence is seen in either image in Figure 8 for the directly mixed carbon black.

The above results support our interpretation of the NMR origin of the artifacts. "Coke" particles are the most likely cause, although small iron or rust particles or perhaps particulate carbon black agglomerates cannot be ruled out totally. In one case of a carbon-black-filled, uncured elastomer where the artifacts were seen, a search for metal particles was unsuccessful. Artifacts such as these can complicate interpretation of NMR images. However, one may be able to identify impurities or defects based on susceptibility artifacts, a point worthy of further study.

Conclusions

We have shown that direct T_2 -weighted, low-TE spin-echo NMR imaging can visualize certain morphologic and defect structures and can differentiate among various layers in actual tire samples with no probing agent. At a

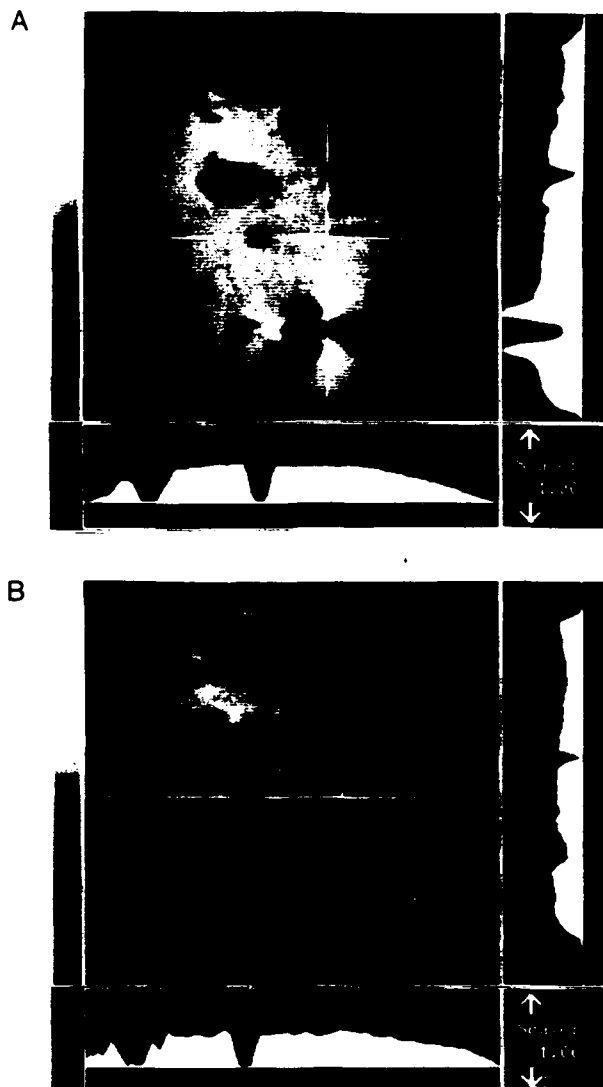


Figure 8. (A) Typical spin-echo, volume image slice of a phantom containing a capillary filled with air (top right), a capillary filled with powdered carbon black (close to center), a graphite pencil tip (lower center), and air pockets visible as irregular defects in a vegetable shortening matrix. Powdered carbon black was mixed with the shortening in the top one-third of the volume. Note the arrowhead artifact around the pencil tip. (B) Gradient-echo image of the same slice. TE, 1.3 ms; TR, 1 s; total time, 1 h in both A and B.

gradient strength of 20 G/cm and a TE of about 1 ms, the T_2 -weighted 3D images can readily differentiate *cis*-BR/SBR diblends which vary in molecular composition by about 20%. Tire treads having differences in carbon black mixing can be differentiated at medium (150- μ m) resolution. Short echo times dramatically improve image quality, and the multislice 3D imaging sequence is a valuable approach for imaging real elastomeric composites, although T_2 weighting is still present in the images of common elastomers. Magnetic susceptibility artifacts frequently appear in the images of filled elastomers and may be a means for identifying various defects based on their magnetic susceptibility differences.

Acknowledgment. We thank Ken Schur of the Uniroyal-Goodyear Tire Co. for providing the samples and for stimulating discussions. We also thank Bob Kadunce of BF Goodrich Co. for valuable discussions of carbon black dispersion and Jim Visintainer of Goodyear Research for discussions about issues in tire characterization. We thank J. Ackerman and L. Garrido of Massachusetts General

Hospital for suggesting magnetic susceptibility differences as the cause of the arrowhead artifacts. We thank Annadell Fowler and John Pearce for running the ^{13}C and ^1H NMR spectra, respectively. This research was funded by Grant AFOSR-89-0418 from the Air Force Office of Scientific Research.

References and Notes

- (1) Listerud, J. M.; Sinton, S. W.; Drobny, G. P. *Anal. Chem.* 1989, 61, 23A.
- (2) Weisenberger, L. A.; Koenig, J. L. *Appl. Spectrosc.* 1989, 43, 1117.
- (3) Clough, R. S.; Koenig, J. L. *J. Polym. Sci., Polym. Lett.* 1989, 27, 451.
- (4) Sarkar, S. N.; Wooten, E. W.; Komoroski, R. A. *Appl. Spectrosc.* 1991, 45, 619.
- (5) Dechter, J. J.; Komoroski, R. A.; Ramaprasad, S. *J. Magn. Reson.* 1991, 93, 142.
- (6) Garrido, L.; Ackerman, J. L.; Ellingson, W. A. *J. Magn. Reson.* 1990, 88, 340.
- (7) Chang, C.; Komoroski, R. A. *Macromolecules* 1989, 22, 600.
- (8) Komoroski, R. A.; Sarkar, S. N. *Proc. Mater. Res. Soc.* 1991, 217, 3.
- (9) Webb, A. G.; Jezzard, P.; Hall, L. D.; Ng, S. *Polym. Commun.* 1989, 30, 364.
- (10) Blümlein, P.; Blümich, B. *Macromolecules* 1991, 24, 2183.
- (11) Miller, J. B. *Trends Anal. Chem.* 1991, 10, 59.
- (12) Cory, D. G.; Miller, J. B.; Turner, R.; Garroway, A. N. *Mol. Phys.* 1990, 70, 331.
- (13) Cory, D. G.; deBoer, J. C.; Veeman, W. S. *Macromolecules* 1989, 22, 1618.
- (14) Frahm, J.; Merboldt, K. D.; Hanicke, W. *J. Magn. Reson.* 1987, 72, 502.
- (15) Komoroski, R. A. In *High Resolution NMR Spectroscopy of Synthetic Polymers in Bulk*; Komoroski, R. A., Ed.; VCH Publishers: Deerfield Beach, FL, 1986; Chapter 4.
- (16) Lee, S. W.; Hilal, S. K.; Cho, Z. H. *Magn. Reson. Imaging* 1986, 4, 343.
- (17) Chang, C.; Komoroski, R. A. In *Solid State NMR of Polymers*; Mathias, L. J., Ed.; Plenum: New York, 1991; in press.
- (18) Chu, S. C.-K.; Xu, Y.; Balschi, J. A.; Springer, C. S., Jr. *Magn. Reson. Med.* 1990, 13, 239.
- (19) Ludeke, K. M.; Roschmann, P.; Tischler, R. *Magn. Reson. Imaging* 1985, 3, 329.
- (20) Kadunce, R. *Rubber Chem. Technol.* 1974, 47, 469.
- (21) Komoroski, R. A. *Rubber Chem. Technol.* 1983, 5, 959.
- (22) Komoroski, R. A.; Mandelkern, L. In *Applications of Polymer Spectroscopy*; Brame, E. G., Ed.; Academic Press: New York, 1987; Chapter 5, p 57.
- (23) Jezzard, P.; Carpenter, T. A.; Hall, L. D.; Jackson, P.; Clayden, N. J. *Polym. Commun.* 1991, 32, 74.
- (24) Vegvari, P. C.; Hess, W. M.; Chirico, V. E. *Rubber Chem. Technol.* 1978, 51, 817.
- (25) Kadunce, R. J.; Smith, R. W. In *Proceedings of the International Symposium for Testing and Failure Analysis*, Los Angeles, Nov 9-13, 1987 (sponsored by ASM International, Metals Park, OH).

NMR Imaging of Water in Model Porous Materials

SUBHENDRA N. SARKAR, E. WRENN WOOTEN,* and
RICHARD A. KOMOROSKI†

Departments of Radiology and Pathology, University of Arkansas for Medical Sciences, Little Rock, Arkansas 72205

Nuclear magnetic resonance images have been obtained for four porous glass disks of different porosities as models of materials such as oil cores. The mottled appearance often seen for such images is attributed largely to insufficient signal-to-noise ratio, and not pore structures. Comparison of spin-echo and gradient-echo images demonstrates the defect-magnification effect of the gradient-echo sequence seen previously for elastomers. The advantages of volume imaging, isotropic voxels in thin slices, and higher resolution are demonstrated for porous materials. Images with isotropic voxels of 80 to 100 μm on a side were obtained in several hours. Dramatic differences are not seen at 100- μm resolution for disks of average pore size 15 to 200 μm because the images are dominated by the large-pore tail of the size distribution.

Index Headings: NMR imaging; Porous materials; Spin relaxation.

INTRODUCTION

Nuclear magnetic resonance (NMR) imaging has seen increasing use in the analysis of materials.¹ Because NMR imaging is primarily a technique for liquids, most work to date has involved imaging ¹H-rich solvents in porous solids or elastomers of high molecular mobility.² Areas of interest have been analysis of oil cores, quality control in the processing of green ceramics, void distributions in composite materials, and solvent diffusion in polymers.

A variety of oil cores have been imaged for rock defects, porosity, and water and oil distribution, and in flow studies.³⁻⁵ Although defects such as cracks and large voids (both accessible and inaccessible to H₂O) were readily seen, the relationship of the NMR image to pore size and its distribution was not apparent because the image pixel size was typically much larger than the pore size, and the slices examined were thick (1-10 mm). The mottled appearance typical of oil core images was also observed for NMR images of homogeneous rubber,² where it was attributed to low signal-to-noise (S/N) ratio in combination with the signal threshold chosen for image display. Benzene-soaked, partially sintered Al₂O₃ disks have been imaged without resolving individual pores.⁶ These workers have also imaged 2.5% polymeric binder in Al₂O₃ green body at 330 \times 330 μm in-plane resolution.⁷

We examine here several aspects of NMR imaging as they apply to porous materials. The effect of resolution relative to the pore size is examined for sintered glass disks of various pore sizes. The value of thin slices and isotropic voxels, either in standard spin-echo (SE) or volume imaging, is demonstrated. As done previously for elastomeric materials,² defect magnification can be obtained with the use of the gradient-echo (GRE) sequence.

EXPERIMENTAL

Samples. Sintered glass disks of various porosities were obtained from Kontes, Vineland, NJ. The disks were about 4 to 5 mm thick and about 6 cm in diameter. From the difference in weight when dry and when fully soaked, the approximate fraction of total volume accessible to water can be obtained. These fractions are listed in Table I for the case when the disks are soaked in air at atmospheric pressure. These proportions were verified approximately by the total spin-echo intensities of the ¹H NMR signals from different disk samples at 4.7 T after normalization of the signals for the various spin-spin relaxation time (T_2) values, assuming an exponential decay.

Imaging at 1.5 T. The whole disks were soaked in deionized water for several hours and clamped into a flat plexiglas holder fitted to the disks. Most residual water was removed, leaving a thin layer below the disks to serve as a source of water to avoid drying during imaging. A flat plate was screwed on top with an O-ring seal to minimize evaporation.

Images were obtained at 63.9 MHz on a General Electric Signa clinical magnetic resonance imaging system with a maximum gradient strength of 1 G/cm. A 5-in. general-purpose surface coil was used to provide the rf field. The entire disk was laid flat on the surface coil at several cm distance to ensure reasonably homogeneous excitation. Radiofrequency field homogeneity was confirmed in one case by comparison to an image using a cylindrical coil. Typically an 8-12-cm field of view and acquisition matrix of 256 \times 128 were used. A single-slice, spin-echo sequence with 1-50 excitations, time to echo (TE) of 20 ms, and pulse sequence delay (TR) between 1000 and 2000 ms was used to image 3-mm-thick slices (the minimum on the Signa) within 4 min to 3 h. Gradient-echo images with flip angles of 20-90°, TE of 11-12 ms, TR of 600-1000 ms, and total imaging time of 17-35 min were also obtained. Basic SE and GRE sequences have been described previously.² Three-dimensional volume images⁸ using a gradient-echo sequence required about one hour to provide a set of 28 images, each for a 1-mm-thick slice.

Spin-lattice relaxation time (T_1) values were measured with the use of a standard inversion recovery sequence under the same conditions as for imaging at 1.5 T, except that a TR of 15 s, six dummy scans, and a 180-90 pulse separation (TI) of 7-1600 ms were used. The spectra were integrated to yield intensities $M(t)$ and the T_1 s extracted from plots of $\ln[M_0 - M(t)]$.

Imaging at 4.7 T. The ¹H images at 4.7 T (200.1 MHz) were collected at a gradient strength of 20 G/cm on a General Electric Omega CSI-4.7 with an Acustar gradient

Received 28 September 1990.

* Current address: Department of Chemistry, University of California, Berkeley, CA 94720.

† Author whom correspondence should be sent.

TABLE I. Pore sizes, water contents, and spin relaxation times for porous disks.

System	Nominal pore size (μm)	Vol. % H_2O saturated	T_1 (ms) at 1.5 T	T_2 (ms) at 4.7 T
Pure water	2700	...
Extra coarse disk	170–220	35	2300	64
Coarse disk	40–60	20	...	56
Medium disk	10–15	24	...	39
Fine disk	4–5.5	40	2100	33

system of 120-mm bore size. An SE sequence was used with 4-lobe, slice-selective sinc 90° and 180° rf pulses, a TE of 14 ms, and a TR of 1000 ms.

Typically 7-mm \times 7-mm \times 5-mm pieces were cut from the above disks and presoaked in deionized water for several hours. A single-turn, 2-cm, G.E. ^1H surface coil was used with a homemade acrylic plastic holder permitting manual positioning of the sample to within an accuracy of 0.1 mm. The fields of view were 10.2 mm (80- μm resolution), 12.8 mm (100- μm resolution), 25.6 mm (200- μm resolution), and 51.2 mm (400- μm resolution), all with data matrix size 128×128 . The slice thicknesses were equal to the in-plane resolution in most cases to give nominally cubic voxels. The imaging times for the extra coarse and fine disks varied between 16 min for the most favorable case (the extra coarse disk at 400- μm resolution) to 4.5 h for the 100- μm images. The medium and coarse disks, which were of lower water content, were imaged in about 9 h at 80- μm resolution. The small disk pieces were wrapped in Teflon[®] tape after soaking and sealed in 10-mm NMR tubes containing a small water reservoir away from the surface coil. This minimized drying of the samples with time. Since the rf excitation of a surface coil falls off with distance, a single parallel plane was chosen at a fixed offset from the plane of the coil, and all imaging slices were chosen relative to that

plane. No attempt was made to compare absolute signal intensities among the slices thus selected. Since there was no large amount of free water trapped in the wrapped samples, related image artifacts were minimized. However, protons from the acrylic holder appeared as a wide hump, creating problems in shimming, particularly for the samples low in water content.

Spin-spin relaxation time (T_2) measurements were performed with the use of the nonlocalized Hahn spin-echo sequence on the entire sample. The TE was varied between 5 and 100 ms, and the total echo magnitudes were plotted against TE and fit to a single exponential decay to give average values for T_2 .

RESULTS AND DISCUSSION

Signal-to-Noise Ratio. Figure 1 shows the effect of S/N ratio on the NMR image of the fine disk. One excitation and a TR of 1000 ms were used in Fig. 1A, where the image has the typical mottled appearance. Fifty excitations and a TR of 1500 ms were used in Fig. 1B, and the image appearance is dramatically smoother. The mottling, which might be interpreted as relating to pore structure, arises from low S/N ratio coupled with a high threshold for image display. A small circular dark spot and larger diffuse regions of lower intensity near the center of the disk are barely visible in Fig. 1A, but are clearly apparent in Fig. 1B. The same is true of the Gibbs artifact at the top and bottom of the image, due to insufficient data sampling in the frequency encode direction. Because it is often not possible to signal average long enough to obtain S/N comparable to that in Fig. 1B, care must be taken in identifying small defect structures under reduced S/N conditions.

Relaxation Times. The bulk T_1 s (at 1.5 T) and T_2 s (at 4.7 T) for the disks are listed in Table I. Both T_1 and T_2 decrease with pore size, as expected. An attempt to relate

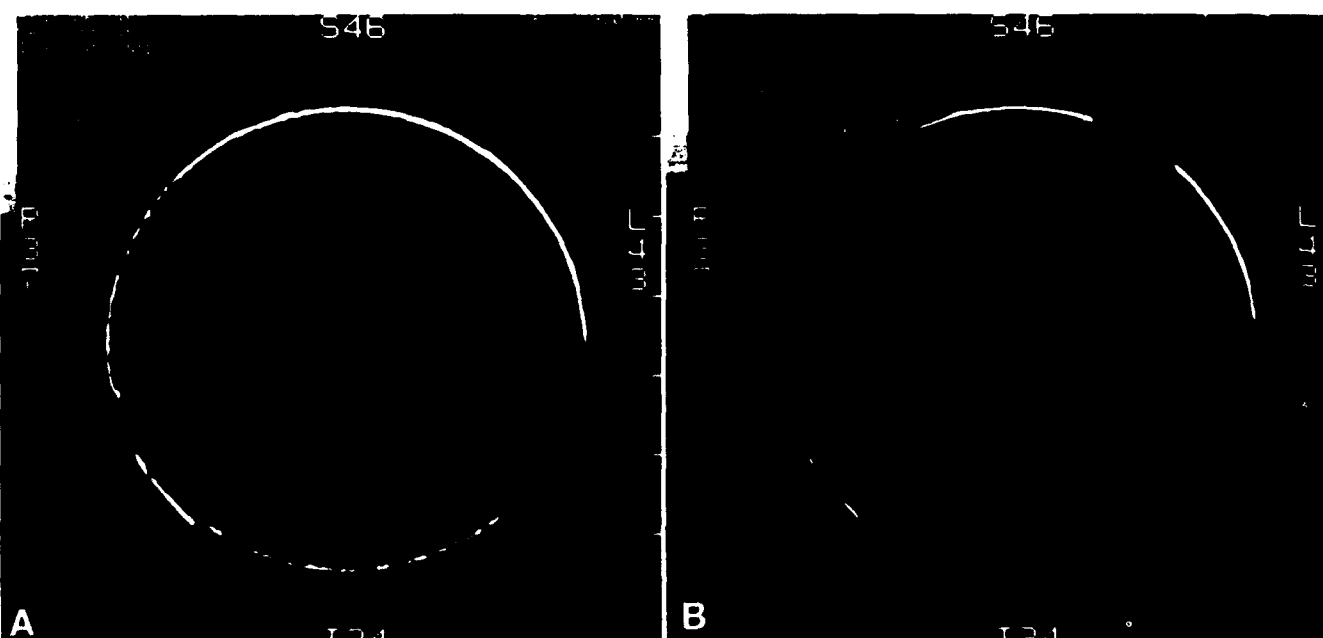


FIG. 1. Spin-echo NMR images of the fine porosity disk at 1.5 T: (A) 1 excitation and TR of 1000 ms; (B) 50 excitations and TR of 1500 ms. The faint arcs at left and bottom right in both images are due to inadequacies of photography on our Signa system and do not involve the image itself.

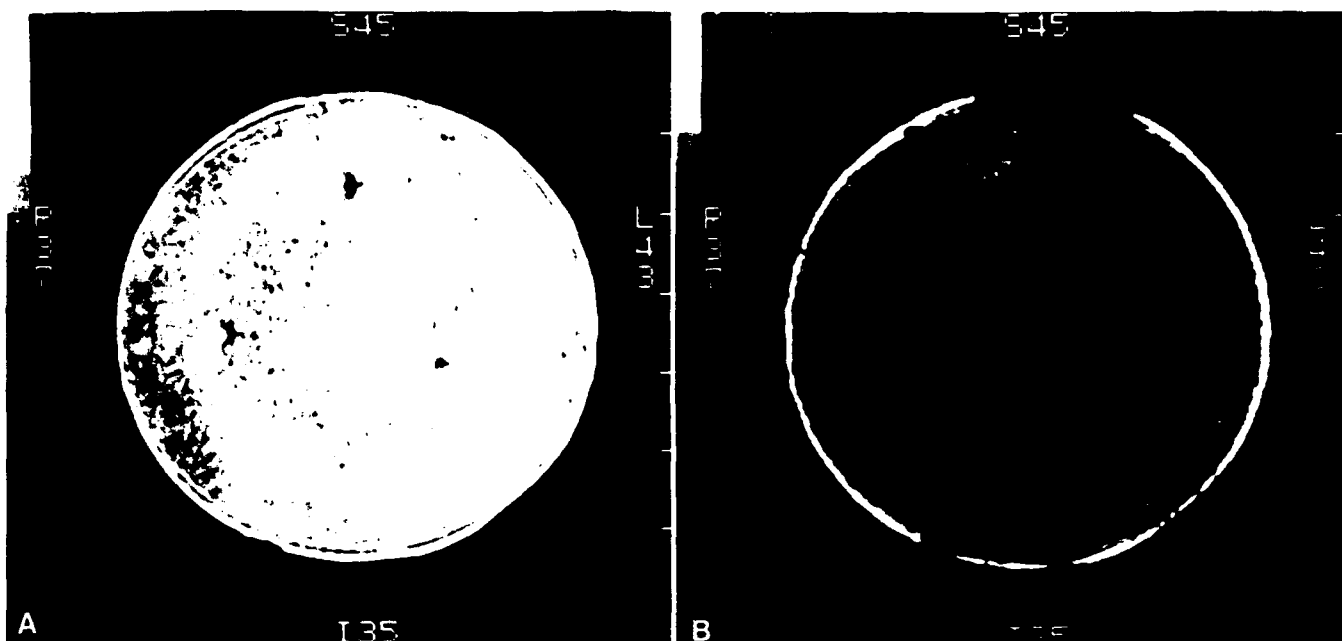


FIG. 2. (A) Spin-echo image ($TE = 20$ ms) of a 3-mm slice through the extra coarse disk at 1.5 T; (B) gradient-echo image ($TE = 15$ ms) of the same slice. Field of view, 8 cm; matrix size, 128×256 ; TR, 1 s; No. of acquisitions, 8; tip angle, 20° .

T_1 or T_2 for the set of disks to pore size using a simple model⁹ was not successful, apparently due to different pore geometries or distributions for the various disks. Images of the extra coarse disk taken at 1.5 T as a function of TR and TE did not reveal any major regional variations of T_1 or T_2 in the slice taken.

Spin-Echo versus Gradient-Echo Images. In GRE images, the rephasing is done by reversal of the read gradient instead of applying a 180° pulse as for the SE sequence. Unlike the case for SE images, magnetic field inhomogeneities and chemical shift effects are not refocused at the echo maximum for GRE images. The intensities in GRE images are determined by T_2^* , the time constant for decay of the FID, and are highly sensitive to differences in magnetic susceptibility of various regions in the sample. Comparative images (Fig. 2) were taken with the SE and GRE sequences at 1.5 T for the extra coarse disk. Numerous defects are observed in the spin-echo image (Fig. 2A), and the central region appears slightly darker due to a lower local concentration of H_2O . The largest defects in the SE image are interesting in that adjacent to them are bright spots from susceptibility artifacts. Considerable detail is seen in the GRE image of the same slice (Fig. 2B). The central region is now substantially darker than the outer region, indicating a reduced T_2^* for the central region. Many more "defects" are clearly seen, even against the mottled background, and the ones seen in the SE image appear enlarged in the GRE image. However, the bright spots near the largest defects are not apparent in the GRE image.

The results of Fig. 2 are similar to those previously obtained for pure elastomers.² The detail in the GRE image for the most part cannot be due to T_2 effects or to direct absence of spin density because these would also be reflected in the spin-echo image. The detail probably arises from magnetic susceptibility variations near void or solid glass particle surfaces, or in regions of dif-

fering pore size or density. Hence water near the surface of the defect will have a shorter T_2^* than more distant H_2O . In a gradient-echo image these surface regions would appear darker, enlarging the apparent size of the defect.² Thus the water giving rise to the bright spots of Fig. 2A has short T_2^* by virtue of its proximity to defects, and appears dark on the GRE image. Such an effect is observed at tissue/air boundaries in medical imaging using gradient-echo sequences.¹⁰

Volume Imaging. Multi-slice SE and GRE techniques are commonly used in medical applications of NMR imaging. However, the minimum slice thickness is limited by the gradient strength, and time-costly interleaving is required if contiguous slices are desired. Although contiguous slices often are not necessary for medical applications, they are very important for materials applications such as oil core profiling.⁵ Three-dimensional volume

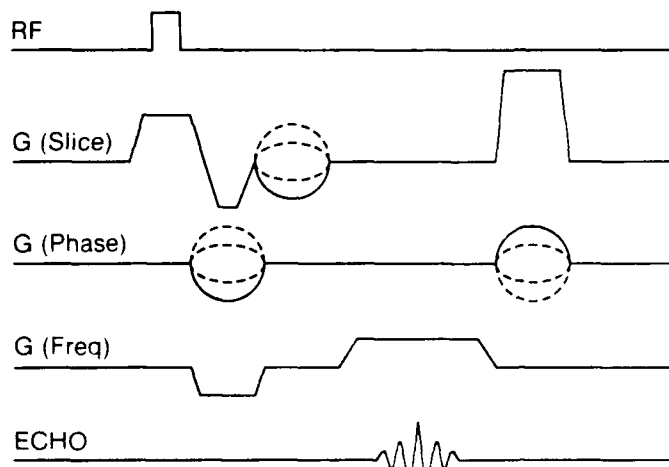


FIG. 3. A basic 3D GRE imaging sequence similar to that used to acquire the images in Fig. 4.

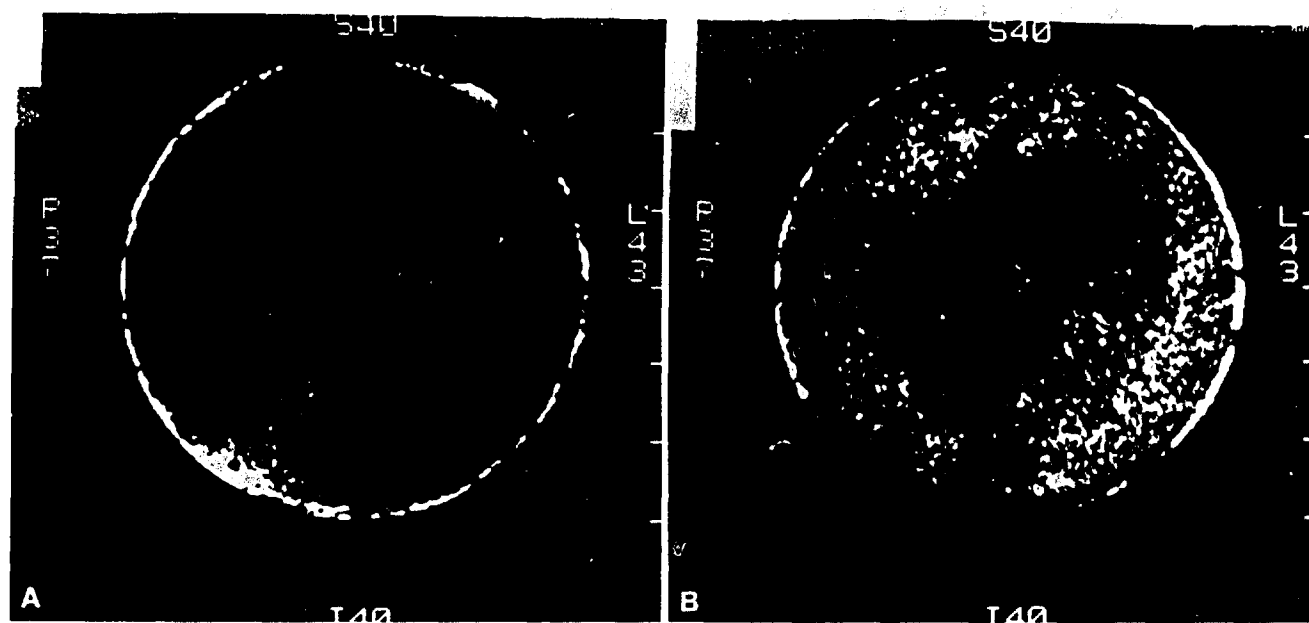


Fig. 4. Two 1-mm thick slices from a 3D, GRE dataset (28 total slices) of the extra coarse disk at 1.5 T; TR, 800 ms; TE, 20 ms; tip angle, 60°; FOV, 8 cm; matrix size, 128×256 ; 1 acquisition.

imaging yields thin, contiguous slices, although currently data acquisition and processing can be time-consuming, at least by medical imaging standards. Such time constraints are not as critical in NMR imaging of materials.

Figure 3 shows a basic 3D imaging sequence with the use of a gradient echo. A thick slab is first excited in the material by simultaneously applying an rf pulse and weak slice-select gradient. Slice selection is performed by stepping a phase-encoding gradient in the slice-select direction. The number of slices is given by the number of slice-select phase encode steps, and the slice thickness is given by the field of view in that direction divided by the number of steps. The technique has been demonstrated for elastomers.

Figure 4 shows two typical 1-mm thick slices from a 3D volume set at 1.5 T for the extra coarse disk. Figure 4A shows clearly the presence of numerous, well-defined defects in that slice. Because of the thinner slice, defects are more well defined in a slice from the 3D dataset. Figure 4B is taken from the same region encompassed by the 3-mm GRE slice of Fig. 2B. For the large feature at the top and center of the disk, one of the bright spots seen on the SE image (Fig. 2A), but not on the thicker-slice GRE image (Fig. 2B), is now apparent.

Higher Gradient Strength and Resolution. Considerable effort is being expended in developing NMR imaging techniques applicable at the microscopic level.¹³⁻¹⁵ Microscopic NMR imaging is expected to play a significant role for materials. The primary instrumental requirement for increased resolution is powerful gradients. The resolution Δx in an NMR image is given by

$$\Delta x = 1/(\gamma G \cdot AT) \quad (1)$$

where γ is the magnetogyric ratio, G is the gradient strength, and AT is the data acquisition time. Figure 5 shows plots of G vs. AT (TE) or linewidth for various Δx values in NMR imaging.

The significance of the acquisition time is that, in echo imaging, it is limited by (and often equal to) the echo time TE. For materials, T_2 can be quite short, and hence TE or AT cannot be lengthened without loss of echo signal.

Another consideration is the resonance linewidth for the material. The spread of frequencies ($\gamma G \Delta x$) caused by the gradient must be larger than the spread inherent

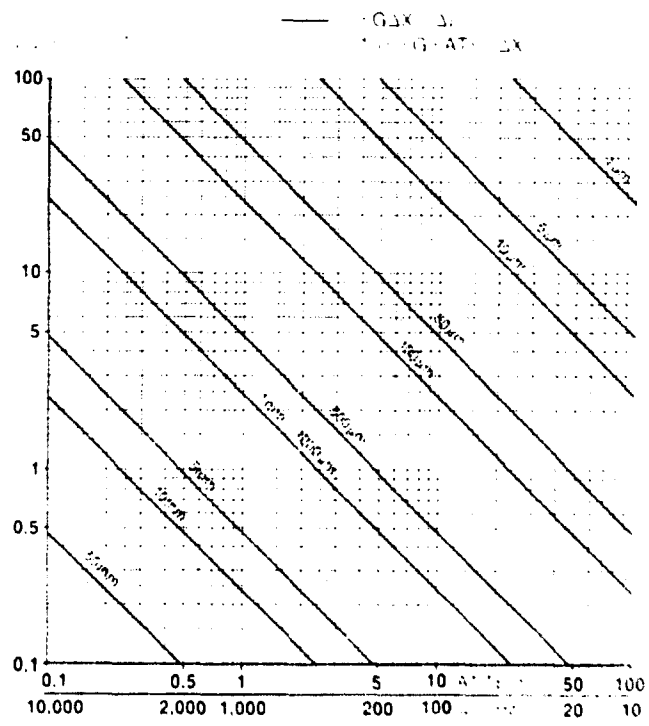


Fig. 5. Plots of G vs. AT (TE) or linewidth for various Δx values in NMR imaging.

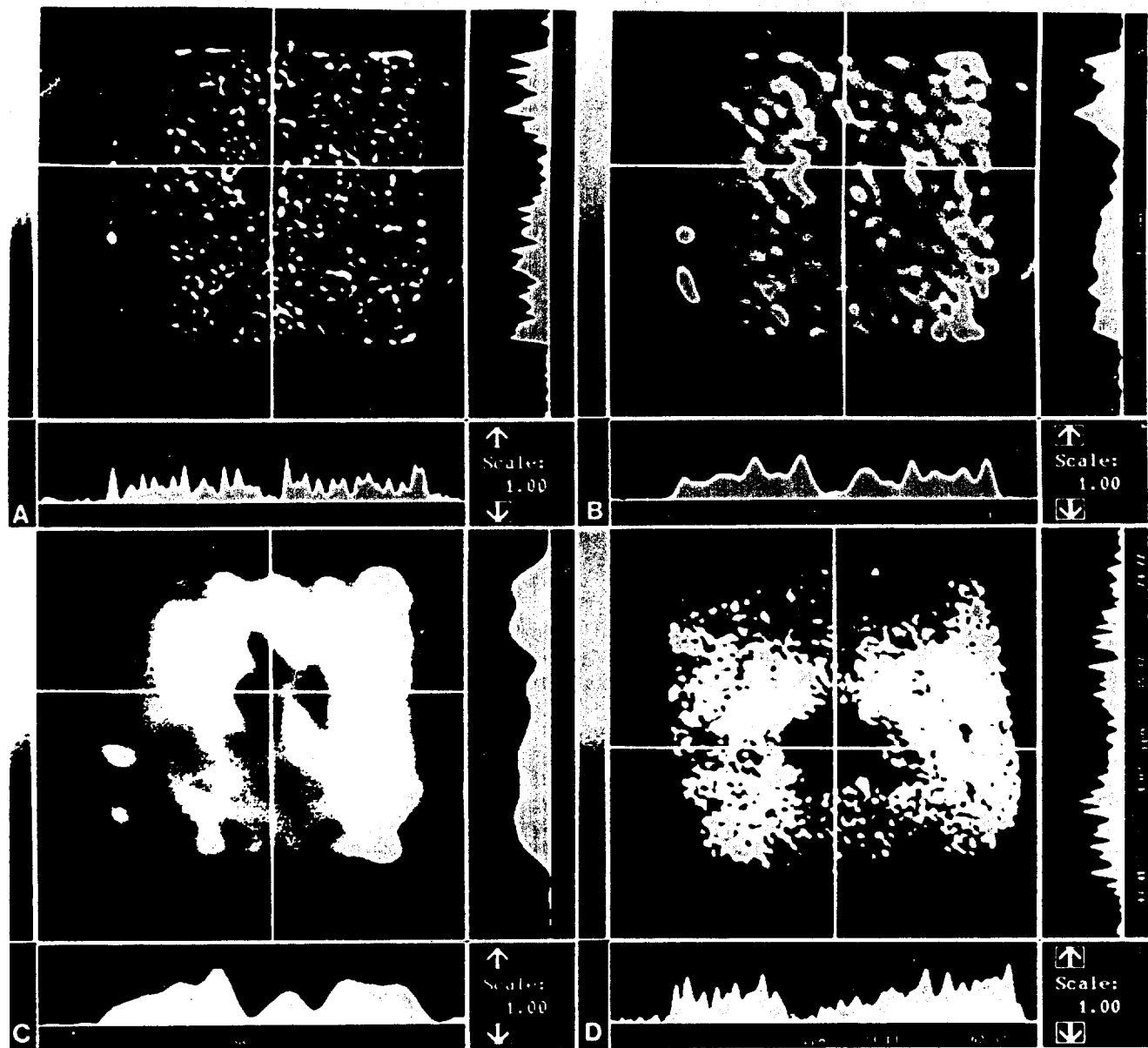


Fig. 6. NMR images at 4.7 T of a 7 × 7 mm portion of the extra coarse disk at three isotropic resolutions: (A) 100 μm ; (B) 200 μm ; and (C) 400 μm ; (D) 100 \times 100 \times 2000 μm voxels. To the bottom and right of the images are intensity profiles of the object at the position of the parallel axis in the image display.

in the line width $\Delta\omega$. This relationship, which is just a different way of expressing Eq. 1, is also shown in Fig. 5. The relatively large linewidths seen for materials also necessitate powerful gradients. At 4.7 T our linewidths were about 250 Hz (fine and extra coarse disks) and 500 Hz (medium and coarse disks), which puts a resolution limit of 35–50 μm at 20 G/cm for these materials.

To date, most NMR imaging of materials has been with highly anisotropic voxels and very poor resolution perpendicular to the slice. The advantage of isotropic voxels for visualizing complex 3D structures and minimizing confusing partial volume effects has been recognized. Although 3D volume imaging may ultimately be the method of choice for obtaining isotropic voxels, it is possible to use the single-slice technique at moderately

good resolution. Figures 6A–C show images (4.7 T, 20 G/cm) of a 7 × 7-mm piece of the extra coarse disk at three different isotropic resolutions—less than, at, and greater than the nominal pore size. As expected, the images are dramatically different and, in particular, display how features in the low-resolution image arise from different planes in the slice. In the 100- μm isotropic-voxel image, there are a few small and intense spots whose size is about 190 $\mu\text{m} \times$ 190 μm in plane and are either single pores or collections of smaller pores. Longer spots may be pores connected in plane. Small and weak spots may be from pores of about 100- μm size or less and fully included in the slice, or from larger pores partially cut by the 100- μm slice. For the 200- μm and 400- μm isotropic-resolution images (Figs. 6B and 6C, respectively), a few

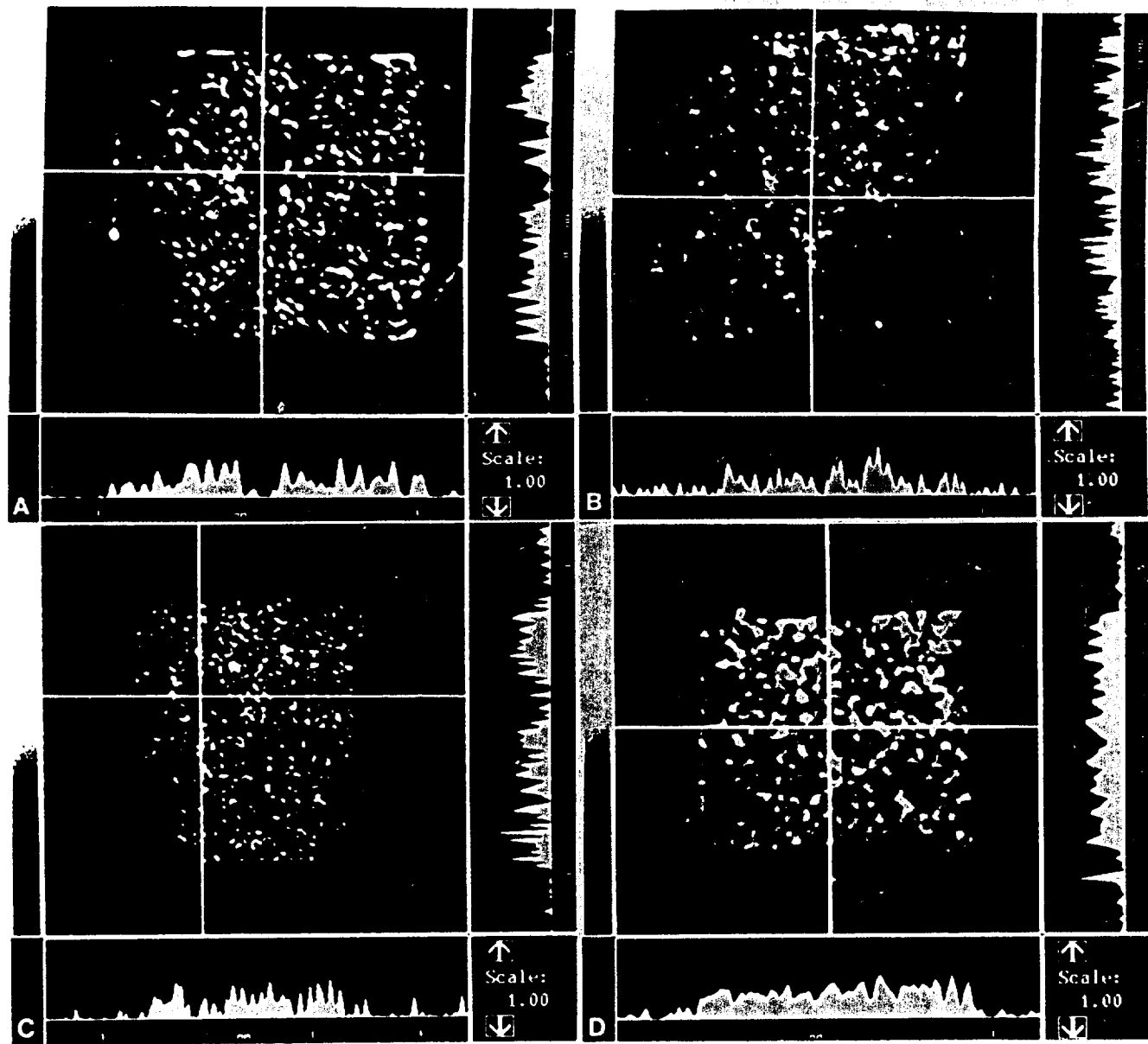


Fig. 6. NMR images at 4.7 T of portions of the (A) extra coarse (100 μm); (B) coarse (80 μm); (C) medium (80 μm); and (D) fine (100 μm) disks.

intense spots become larger as the resolution becomes coarser. Some of the spots remain bright, implying perhaps collections of water-filled pores from various planes. The extra coarse disk seems to be very heterogeneous in pore size and connectivity.

The higher-resolution appearance of Fig. 6A is retained to a large extent in Fig. 6D, an image with 100 \times 100 \times 2000- μm voxels, even though features from the equivalent of 20,100- μm slice thicknesses contribute to the latter image. This arises from the fact that the majority of the object volume is occupied by glass, and hence a relatively large number of the anisotropic voxels have little or no signal. For porous materials of low-to-medium porosity, thick slices may provide more useful information than for relatively homogeneous materials such as polymers.

The results of Fig. 6 also demonstrate that obtaining isotropic voxels at high resolution will not exact too severe a penalty in S/N ratio for porous materials. Although the voxel volume in the 100- μm image is 1/64th that of the 400- μm image, it took only 16 times (4 \times S/N penalty) as long to obtain the 100- μm image. This arises from the "dilution" of the signal by glass as the resolution becomes coarser.

Figure 7 shows images of portions of all the disks at 4.7 T under comparable conditions and with isotropic voxels at moderate resolution. The image of the fine disk (Fig. 7D) has a more homogeneous distribution of intensities than the other disks. The sizes of the spots are not more than 160 μm and obviously not less than 100 μm . We are observing either many fine pores or the tail of a pore size distribution containing at most 160- μm pores.

or both. The images of the other three disks are in general similar in appearance among themselves. For the medium and coarse disks, the appearance is strongly influenced by the low S/N ratio. However, the lack of dramatic difference at 100- μm resolution suggests that the role of pores smaller than the pixel size is ambiguous. If the distribution of pores is homogeneous at an intermediate spatial scale (100–1000 μm) in the first three disks, then the image is probably dominated by the large-pore tail of the distribution.

The above images were obtained in signal averaging times of up to about 4 h. With additional signal averaging, usable images of lower S/N ratio could be obtained for isotropic voxels of 40 μm for the extra coarse and fine disks under our conditions.

CONCLUSIONS

The results presented here demonstrate the following:

1. The mottled appearance of images of porous materials can be due to inadequate S/N.
2. Images of 80- μm resolution can be observed by SE imaging in a few hours at 17–40°C H_2O .
3. GRE imaging can provide a magnification effect for defects in porous materials.
4. Isotropic voxels at moderately high resolution yield superior images for porous materials with only a modest S/N penalty.
5. The NMR images of materials with wide porosity distributions may appear similar because they are dominated by the large-pore tail of the distribution.

ACKNOWLEDGMENTS

We thank Prof. Bill Ritchey for suggesting the sintered glass disks as models. This research was funded by Grant AFOSR-89-0418 from the Air Force Office of Scientific Research.

1. J. M. Listerud, S. W. Sinton, and G. P. Drobny, *Anal. Chem.* **61**, 23A (1989).
2. C. Chang and R. A. Komoroski, *Macromolecules* **22**, 600 (1989).
3. W. A. Edelstein, H. J. Vinegar, P. N. Tutunjian, P. E. Roemer, and O. M. Mueller, *SPE Preprint* **18272**, 101 (1988).
4. B. A. Baldwin and W. S. Yamanashi, *Magn. Reson. Imaging* **6**, 493 (1988).
5. J. J. Dechter, R. A. Komoroski, and S. Ramaprasad, *Proc. Soc. Core Analysts*, #8903 (1989).
6. W. A. Ellingson, P. S. Wong, S. L. Dieckman, J. L. Ackerman, and L. Garrido, *Cer. Bull.* **68**, 1180 (1989).
7. L. Garrido, J. L. Ackerman, and W. A. Ellingson, *J. Magn. Reson.* **88**, 340 (1990).
8. P. G. Morris, *Nuclear Magnetic Resonance Imaging in Medicine and Biology* (Clarendon Press, Oxford, 1986).
9. D. P. Gallegos, K. Munn, D. M. Smith, and D. L. Stermer, *J. Colloid Interface Sci.* **119**, 127 (1987).
10. E. M. Haacke and E. M. Bellon, in *Magnetic Resonance Imaging*, D. D. Stark and W. G. Bradley, Eds. (C. V. Mosby, St. Louis, 1988), Chap. 8, p. 138.
11. F. W. Wehrli, in *Magnetic Resonance Imaging*, D. D. Stark and W. G. Bradley, Eds. (C. V. Mosby, St. Louis, 1988), Chap. 1, p. 3.
12. C. Chang and R. A. Komoroski, in *Solid State NMR of Polymers*, L. R. Mathias, Ed. (Plenum, New York, 1991).
13. C. D. Eccles and P. T. Callaghan, *J. Magn. Reson.* **68**, 393 (1986).
14. J. B. Aguayo, S. J. Blackband, J. Schoeniger, M. A. Mattingly, and M. Hintermann, *Nature (London)* **322**, 190 (1986).
15. X. Zhou, C. S. Potter, P. C. Lauterbur, and B. Voth, *Abstracts, Eighth Annual Meeting, Soc. Magn. Reson. Med.*, 286, (1989).